A&A 663, A125 (2022)
https://doi.org/10.1051/0004-6361/202142645

Astronomy & Astrophysics

[Mg/Fe] ratios in the solar neighbourhood: Stellar yields and chemical evolution scenarios⋆

Marco Palla[1,2,3], Pablo Santos-Peral[4,5], Alejandra Recio-Blanco[4], and Francesca Matteucci[1,2,6]

[1] INAF – Osservatorio Astronomico di Trieste, Via G.B. Tiepolo 11, 34131 Trieste, Italy
e-mail: marco.palla@inaf.it
[2] Dipartimento di Fisica, Sezione di Astronomia, Universitá di Trieste, Via G.B. Tiepolo 11, 34131 Trieste, Italy
[3] Sterrenkundig Observatorium, Ghent University, Krijgslaan 281 – S9, 9000 Gent, Belgium
[4] Université Côte d'Azur, Observatoire de la Côte d'Azur, CNRS, Laboratoire Lagrange, Bd de l'Observatoire, CS 34229, 06304 Nice cedex 4, France
[5] Departamento de Física de la Tierra y Astrofísica, Universidad Complutense de Madrid, 28040 Madrid, Spain
[6] INFN – Sezione di Trieste, Via Valerio 2, 34100 Trieste, Italy

Received 11 November 2021 / Accepted 25 April 2022

ABSTRACT

Context. The [Mg/Fe] abundance ratios are a fundamental fossil signature used to trace the chemical evolution of the disc and to divide it into low-α and high-α populations. Despite the huge observational and theoretical efforts, discrepancies between models and data are still present and several explanations have been put forward to explain the [α/Fe] bimodality.
Aims. In this work we take advantage of a new AMBRE:HARPS dataset, which provides new more precise [Mg/Fe] estimations and reliable stellar ages for a subsample of stars, to study the [α/Fe] bimodality and the evolution of the solar neighbourhood.
Methods. The data are compared with detailed chemical evolution models for the Milky Way, exploring the most used prescriptions for stellar yields and different formation scenarios for the Galactic disc (i.e. the delayed two-infall and the parallel models), including prescriptions for stellar radial migration.
Results. We see that most of the stellar yield prescriptions struggle to reproduce the observed trend of the data and that semi-empirical yields describe best the [Mg/Fe] evolution in the thick and thin discs. In particular, most of the yields still predict a steeper decrease of the [Mg/Fe] ratio at high metallicity than shown by the data. The bulk of the data are well reproduced by the parallel and two-infall scenarios, but both scenarios have problems in explaining the most metal-rich and metal-poor tails of the low-α data. These tails can be explained in light of radial migration from the inner and outer disc regions, respectively.
Conclusions. Despite the evidence of stellar migration, it is difficult to estimate the actual contribution of stars from other parts of the disc to the solar vicinity in the data we adopt. However, the comparison between data and models suggests that peculiar histories of star formation, such as that of the two-infall model, are still needed to reproduce the observed distribution of stars.

Key words. Galaxy: abundances – Galaxy: disk – Galaxy: evolution – nuclear reactions, nucleosynthesis, abundances

1. Introduction

Our current understanding of the formation and evolution of our Milky Way (MW) disc is mostly based on the study and interpretation of signatures imprinted in stellar populations. In particular, the stellar atmospheres of non-evolved stars inform us about metals in the interstellar medium (ISM) at the time of their formation (Freeman & Bland-Hawthorn 2002), and for decades has been the main source of information regarding the formation and evolution of our own Galaxy.

The [α/Fe] versus metallicity [M/H] (or [Fe/H]) diagram provides valuable clues to the MW disc evolution. The analysis of large survey data, such as APOGEE (e.g., Hayden et al. 2015; Ahumada et al. 2020), GALAH (e.g., Buder et al. 2019), *Gaia*-ESO (e.g., Recio-Blanco et al. 2014; Rojas-Arriagada et al. 2016), and the AMBRE project (e.g., Mikolaitis et al. 2017) suggests the existence of a clear distinction between two sequences of stars in the [α/Fe] versus [Fe/H] space, which are called the high-α sequence (often associated with the thick disc) and the low-α sequence (associated with the thin disc[1]). The significance of this division is even enhanced by the arrival of new dimensions in the data space, such as accurate stellar ages (e.g., from asteroseismology, Pinsonneault et al. 2014, 2018; Miglio et al. 2021) as well as the kinematics and dynamical properties provided by the *Gaia* mission (Gaia Collaboration 2016, 2018, 2021).

However, the origin and shape of this bimodality is still a matter of debate. Several theoretical models suggested that the bimodality may be strictly connected to a delayed gas accretion episode. For example, by revising the classical two-infall chemical evolution model by Chiappini et al. (1997), Spitoni et al. (2019, 2020) shows that a significant delay (4–5 Gyr) between two consecutive episodes of gas accretion is needed to explain the dichotomy in a local stellar sample from APOKASC (Silva Aguirre et al. 2018). Similar conclusions are

⋆ [Mg/Fe] and age values are only available at the CDS via anonymous ftp to cdsarc.u-strasbg.fr (130.79.128.5) or via http://cdsarc.u-strasbg.fr/viz-bin/cat/J/A+A/663/A125

[1] It is worth recalling however that the chemical and geometrical separations give rise to rather different groups (Minchev et al. 2019, see also Caffau et al. 2021; Romano et al. 2021). Therefore, from now on we refer only to the high-α and low-α sequences.

found in Palla et al. (2020b) and Spitoni et al. (2021), where this scenario is extended to the entire MW disc by comparison with the APOGEE data. A late second gas accretion after a prolonged period with a quenched star formation rate (SFR) has also been suggested by the dynamical models of Noguchi (2018) and in cosmological simulations (e.g., Grand et al. 2018; Mackereth et al. 2018). In this framework, Buck (2020) explains the dichotomy as the consequence of a gas-rich merger occurring at a certain epoch in the evolution of the Galaxy (as first proposed in a cosmological model by Calura & Menci 2009).

On the other hand, Grisoni et al. (2017) test the possibility of a picture where high-α and low-α discs are described by two separate and coeval evolutionary sequences (i.e. the parallel scenario). This scenario has been found to be particularly effective to explain the presence of a high-α metal-rich (HαMR) stellar population seen in the AMBRE (e.g., Mikolaitis et al. 2014) and in LAMOST (Sun et al. 2020) data. In the framework of hydrodynamical simulations, the two distinct evolutionary sequences are explained in terms of disc fragmentation: the high-α sequence is attributed to clumps of star formation with high star formation efficiency, whereas the low-α sequence originates from a more distributed and less efficient star formation episode, as shown in Clarke et al. (2019).

The overall picture on MW disc evolution is further complicated by the existence of stellar radial migration, which is theoretically well established (e.g., Sellwood & Binney 2002; Schönrich & Binney 2009; Minchev et al. 2011; Di Matteo et al. 2013) and has been traced in different stellar spectroscopic surveys (e.g., Kordopatis et al. 2015; Hayden et al. 2017; Minchev et al. 2018; Feltzing et al. 2020). In particular, the presence of stars with very high metallicity ([M/H] $\gtrsim 0.1$ dex) and circular orbits at solar radius has been interpreted as clear evidence of stellar migration from inner regions of the Galaxy. However, the real impact of radial migration on the chemical evolution of the Galactic disc is still under debate. For example, Sharma et al. (2021) presented chemical evolution models[2] where the [α/Fe] dichotomy can be reproduced in terms of both the sharp fall in [α/Fe] due to the onset of Type Ia SNe and stellar radial migration. In particular, the high-α sequence is seen as a series of stars with different stellar ages, while the low-α sequence is mostly a series of stars with different birth radii. On the contrary, chemical evolution models by Johnson et al. (2021) including stellar migration failed to match the observed [α/Fe] distribution, indicating that models with smooth star formation histories (SFHs) miss reproducing the α-bimodality (see also Vincenzo et al. 2021). In addition, the results of recent chemo-dynamical simulations has raised doubts about the importance of radial stellar migration in the evolution of abundance ratios in the Galactic disc (e.g., Vincenzo & Kobayashi 2020; Khoperskov et al. 2021), suggesting that the [α/Fe] bimodality is strictly either linked to different star formation regimes or different accretion episodes over the Galaxy lifetime.

In this paper we contribute to this field by comparing detailed chemical evolution models for the solar vicinity with the new local ($d_{\rm sun} < 300$ pc) [Mg/Fe] data from Santos-Peral et al. (2020, 2021). Santos-Peral et al. (2020) carried out an optimised normalisation procedure for stellar spectra which lead to a decreasing [Mg/Fe] trend at supersolar metallicities, at variance with previous works showing a flat trend for the metal-rich ([M/H] > 0) disc (e.g., Adibekyan et al. 2012; Hayden et al. 2017; Buder et al. 2019).

The comparison of this new dataset with the chemical evolution model is manifold. First of all, we explore how different stellar yield sets behave in reproducing the abundances of Santos-Peral et al. (2020, 2021). In fact, Mg is usually used as an α-element tracer (e.g., Mikolaitis et al. 2014; Carrera et al. 2019) because of its simple detection in optical spectra, but its modelling in high-mass star ejecta often produces chemical evolution tracks inconsistent with the observations (see e.g., Romano et al. 2010; Prantzos et al. 2018). Furthermore, we compare the data with different scenarios of chemical evolution proposed for the solar neighbourhood by adopting the parallel model (Grisoni et al. 2017) and the delayed two-infall model (Spitoni et al. 2019; Palla et al. 2020b) in order to highlight their strengths and weaknesses. In light of these two scenarios, we also consider the possible impact of stellar migration on this local sample of stars. To this end, we implement literature prescriptions for radial migration (from Spitoni et al. 2015; Frankel et al. 2018) within our model frameworks. In this way, we test which pathways are likely to explain the star candidates to be migrated from the inner and outer disc.

The paper is organised as follows. In Sect. 2 the observational data adopted are presented. In Sect. 3, we present the main characteristics of the model scenarios, and the adopted stellar yields and radial migration prescriptions. In Sect. 4 we show our results and discuss their implications. Finally, in Sect. 5 we draw our conclusions.

2. The AMBRE:HARPS observational data sample

The AMBRE Project (de Laverny et al. 2013) is a collaboration between the Observatoire de la Côte d'Azur (OCA) and the European Southern Observatory (ESO) to automatically and homogeneously parametrise archived stellar spectra from ESO spectrographs: FEROS, HARPS, and UVES. The stellar atmospheric parameters ($T_{\rm eff}$, $\log(g)$, [M/H], [α/Fe]) were derived by the multi-linear regression algorithm MATrix Inversion for Spectrum SynthEsis (MATISSE; Recio-Blanco et al. 2006), also used in the *Gaia* Radial Velocity Spectrometer (RVS) analysis pipeline (see Recio-Blanco et al. 2016), using the AMBRE grid of synthetic spectra (de Laverny et al. 2012).

For the present paper we only considered the AMBRE:HARPS stellar sample[3], which corresponds to stars in the solar neighbourhood observed at high spectral resolution ($R \sim 115\,000$, described in De Pascale et al. 2014). We adopted the abundance data for 1066 stars from the samples of Santos-Peral et al. (2020, 2021; hereafter S20 and S21). These stars were selected to have $T_{\rm eff} > 4700$ K as cooler stars could have larger errors in the parameters (cf. Fig. 12 in De Pascale et al. 2014). The sample consists of mostly dwarfs ($3.3 \lesssim \log g \leq 4.75$ cm s^{-2}) cooler than 6200 K, whose external uncertainties (estimated by comparison with external catalogues) on $T_{\rm eff}$, $\log(g)$, [M/H], [α/Fe], and $v_{\rm rad}$ are 93 K, 0.26 cm s^{-2}, 0.08 dex, 0.04 dex, and 1 km s^{-1}, respectively. Relative errors from spectra to spectra are much lower. In addition, the stellar [Mg/Fe] abundances were derived following the described methodology in S20, where the spectral normalisation

[2] Actually, they presented empirical age–abundance relations for different radii, whose behaviour has not been demonstrated to be consistent with the assumed SFR evolution (see also Spitoni et al. 2021; Johnson et al. 2021).

[3] The AMBRE analysis of the HARPS spectra comprises the observations collected from October 2003 to October 2010 with the HARPS spectrograph at the 3.6m telescope at the La Silla Paranal Observatory, ESO (Chile).

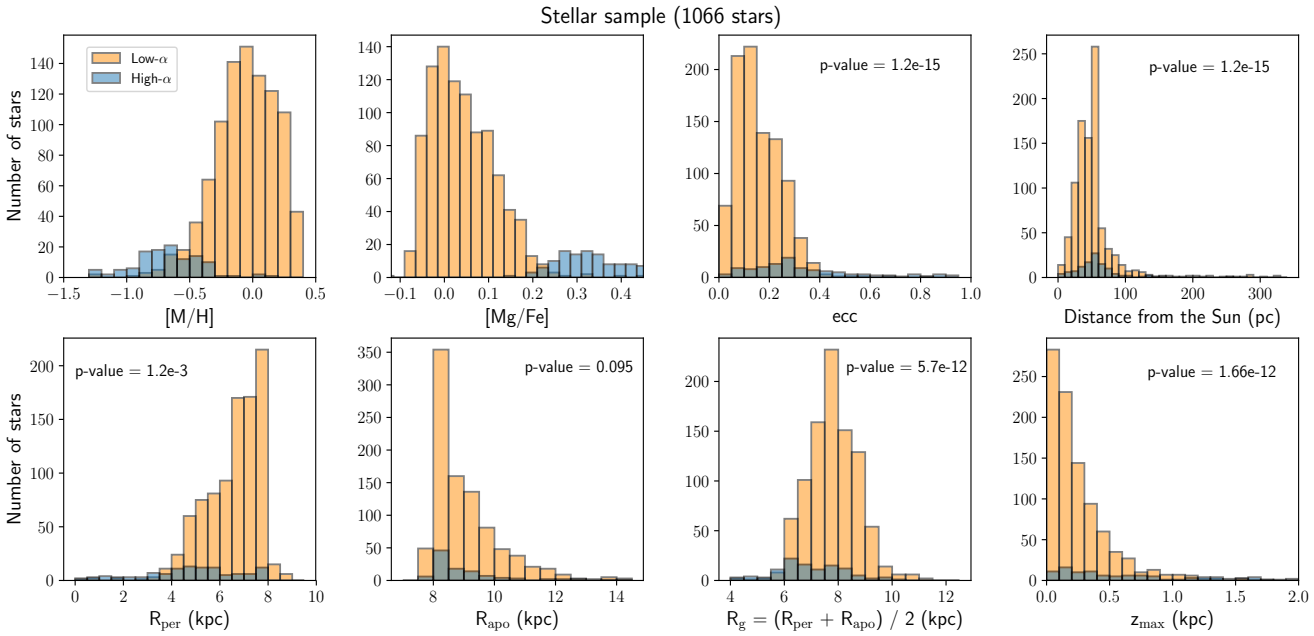

Fig. 1. Distribution of the main properties ([M/H], [Mg/Fe], eccentricity, distance, $R_{\rm per}$, $R_{\rm apo}$, R_g, $z_{\rm max}$) of the stellar sample, separated into the chemically defined low-α (orange) and high-α (blue) disc populations. The p-values of the two-sample Kolmogorov–Smirnov tests are shown for the dynamical properties distributions.

procedure was optimised for the different stellar types and each particular Mg line separately. They present an overall internal error of around 0.02 dex and an average external uncertainty of 0.01 dex with respect to four identified *Gaia*-benchmark stars (18 Sco, HD 22879, the Sun, and τ Cet) from Jofré et al. (2015).

It is worth noting that the [M/H] atmospheric parameter is assumed to be equal to the iron abundance value ([Fe/H]) of the star. The notation comes from the atmosphere models. The four-dimensional synthetic spectra grid, used as a reference in the analysis includes variations in $T_{\rm eff}$, log g, [M/H], and [α/Fe]. In this grid the individual abundance of all non-α chemical elements (e.g., Fe, Cr, Eu) is equal to $[{\rm X}_{\rm non-\alpha}/{\rm H}] = [{\rm M/H}]$. On the other hand, the individual abundance of all the α-elements $[{\rm X}_\alpha/{\rm H}]$ is scaled following the [α/Fe] dimension, $[{\rm X}_\alpha/{\rm H}] = [\alpha/{\rm Fe}] + [{\rm Fe/H}]$, and is taken into account in the estimation of [M/H] through an iterative process (Recio-Blanco et al. 2006, 2016). During the [M/H] estimation, all the non-α metallicity indicators in the observed spectra are considered. These indicators are generally dominated by Fe lines in the optical, as in the case of the AMBRE:HARPS sample. As a consequence, the estimated [M/H] value follows the [Fe/H] abundance with a tight correlation. This is illustrated in Fig. 9 of De Pascale et al. (2014), showing the correlation of the AMBRE:HARPS [M/H] parameter with the estimated [Fe/H] abundance by an independent group (see e.g., Sousa et al. 2008, 2011a,b; Adibekyan et al. 2012) for the same HARPS spectra. Therefore, in the following results and the corresponding interpretation with the chemical evolution models of the [Mg/Fe] versus [M/H] plane, we can assume that [M/H] actually behaves as [Fe/H].

Regarding the [Mg/Fe] abundance estimates, S20 showed a significant improvement in precision by carrying out an optimisation of the spectral normalisation procedure, in particular for the metal-rich population ([M/H] > 0). The followed methodology made it possible to highlight a decreasing trend in the [Mg/Fe] abundance even at supersolar metallicites, partly solving the apparent discrepancies between the observed flat trend in the metal-rich disc (Adibekyan et al. 2012; Hayden et al. 2015, 2017; Buder et al. 2019), and the steeper slope predicted by chemical evolution models (Chiappini et al. 1997; Romano et al. 2010; Spitoni et al. 2020; Palla et al. 2020b). In this paper we directly compare these observational data with the new updated chemical evolution models developed by Palla et al. (2020b) in order to draw more robust conclusions of the Galactic disc evolution scenario.

2.1. Orbital properties and stellar ages

As described in S21, a cross-match of the whole AMBRE:HARPS database with the *Gaia* DR2 catalogue (Gaia Collaboration 2018) was performed in order to use the accurate astrometric (Lindegren et al. 2018) and photometric (Evans et al. 2018) data, along with the estimated distances by Bailer-Jones et al. (2018) from *Gaia* DR2 parallaxes, to estimate the orbital parameters and ages of the stars.

Figure 1 shows the distribution of the main stellar properties of the data sample. These are Galactic disc stars describing relatively circular prograde orbits ($0 < e \lesssim 0.4$) close to the Galactic plane ($|z_{\rm max}| \lesssim 1$ kpc) and in the solar vicinity region ($d \lesssim 300$ pc). We used the guiding centre radius ($R_{\rm g}$), which was calculated as the average between the pericentre and the apocentre of the orbit of the star, $R_g = (R_{\rm per} + R_{\rm apo})/2$, as an estimate of the current value of the galactocentric radius ($R_{\rm GC}$). The sample is well distributed in galactocentric R_g from 4 to 11 kpc. As the analysed sample is very close to the Sun, the new astrometric information from *Gaia* EDR3 (Gaia Collaboration 2021) will not significantly affect our results.

Moreover, we have reliable age values for a subsample of 366 main sequence turn-off (MSTO) stars, estimated using an isochrone fitting method (Kordopatis et al. 2016) with PARSEC isochrones (Bressan et al. 2012). The age distribution for our data subsample ranges from 2.5 to 13.5 Gyr, with an average

relative standard deviation of $\sigma \sim 20\%$ (see complete description in S21).

2.2. Disc chemical distinction

Here we adopt a chemical separation of the Galactic disc components, based on the [Mg/Fe] content in a given [M/H] bin. Figure 2 shows the complete sample from S20 and S21 classified into high-α and low-α sequences. The separation was defined by looking at the gaps in the observed [Mg/Fe] distribution functions in different metallicity bins (of 0.1 dex width) and by performing a linear fit on these divisions (similarly to Adibekyan et al. 2012; Mikolaitis et al. 2017). To evaluate the reliability of this division into low- and high-α disc populations, we performed a Kolgomorov–Smirnov (KS) test between the divided samples to see if the hypothesis that the two populations are drawn from the same underlying population can be excluded (see Fig. 1). In particular, we looked at the dynamical properties (i.e. eccentricity, maximum height above the disc plane, and guiding radius of the orbit) of the stars. The resulting p-values are extremely low (around $<10^{-10}$), confirming that the two populations are actually detached.

We also tried to perform other separations. For example, we selected old stars ($t > 12$ Gyr that would trace the thick disc population, e.g., Haywood et al. 2013) from the MSTO subsample with stellar ages available, and we drew the lower [Mg/Fe]-bound fit to these stars to define the two sequences. However, as discussed in S21, the result of the KS test on stars with intermediate to high metallicity ([M/H] > -0.3 dex) does not allow us to reject the hypothesis of a common origin for the two defined α populations.

In any case, we note that our chosen separation is rather arbitrary and can assume different shapes and/or slopes by looking at different data samples; its function is just to give an idea of the high-α and low-α sequences in the abundance diagram plane. Nevertheless, the results given by the KS test confirm the reliability of this division.

3. Chemical evolution models

In this section we present the chemical evolution models adopted in this work. To follow the chemical evolution of the solar neighbourhood, we adopt two different scenarios in order to highlight their advantages and disadvantages in explaining the chemical history of the solar annulus. In the models, this is assumed to be a 2 kpc wide ring centred at $R = 8$ kpc. The models are described below.

– The delayed two-infall model (Palla et al. 2020b) assumes that the MW disc forms by means of two sequential infall episodes. The first infall give rise to the high-α sequence, whereas the second (delayed and slower) infall forms the low-α stars. With respect to the classical two-infall paradigm (Chiappini et al. 1997; Romano et al. 2010), the second infall is delayed by 3.25 Gyr instead of 1 Gyr. The assumption of a delayed second infall allowed us to reproduce abundance diagrams (Palla et al. 2020b; Spitoni et al. 2021) in the MW disc as well as asteroseismic stellar age trends (Spitoni et al. 2019, 2020) in the solar neighbourhood;

– The parallel model (Grisoni et al. 2017) assumes that the two sequences of stars in the chemical space form from two separate infall episodes, which evolve independently from different gas reservoirs. As in the two-infall model, the infall episode forging high-α stars happens on shorter timescales than that forming low-α stars. This model was tested to reproduce abundance ratios in the solar neighbourhood (Grisoni et al. 2017).

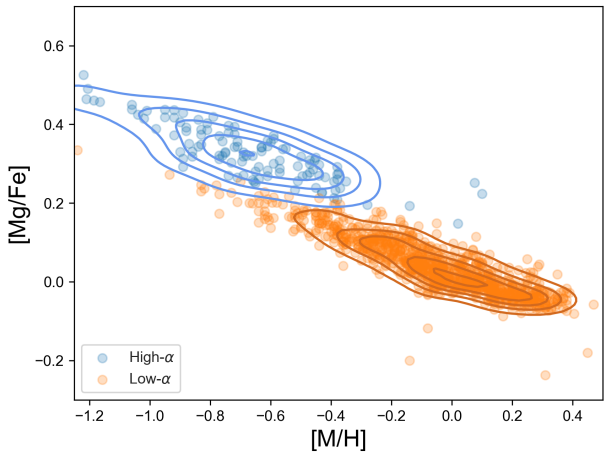

Fig. 2. [Mg/Fe] vs. [M/H] abundance diagram for the sample presented in Santos-Peral et al. (2020, 2021). The light blue dots are the observed high-α stars, whereas the orange dots are the observed low-α stars. The blue and brown contour lines are the density lines of the observed high-α and low-α stellar distributions, respectively.

For both of these chemical evolution models the basic equations that describe the chemical evolution of a given element i are

$$\dot{G}_i(R,t) = -\psi(R,t)X_i(R,t) + R_i(R,t) + \dot{G}_{i,inf}(R,t), \quad (1)$$

where $G_i(R,t) = X_i(R,t)\,G(R,t)$ is the fraction of the gas mass in the form of an element i with $G(R,t)$ the fractional gas mass and $X_i(R,t)$ the abundance fraction in mass of a given element i, with the summation over all elements in the gas mixture being equal to unity.

The first term on the right-hand side of Eq. (1) corresponds to the rate at which an element i is removed from the ISM due to star formation. The SFR is parametrised according to the Schmidt-Kennicutt law (Kennicutt 1998),

$$\psi(R,t) = \nu\,\Sigma_{\rm gas}(R,t)^k, \quad (2)$$

where $\Sigma_{\rm gas}$ is the surface gas density, $k = 1.5$ is the law index, and ν is the star formation efficiency (SFE). This parameter is set to 2 Gyr^{-1} for the first infall–high-α star formation episode and to 1 Gyr^{-1} for the second infall–low-α episode.

The quantity $R_i(R,t)$ (see Palla et al. 2020a for the complete expression) takes into account the nucleosynthesis from low-intermediate mass stars (LIMS, $m < 8\,M_\odot$), core collapse (CC) SNe (Type II and Ib/c, $m > 8\,M_\odot$), and Type Ia SNe (SN Ia). For the SN Ia, we assume the single-degenerate (SD) scenario and in particular the delay-time-distribution (DTD) by Matteucci & Recchi (2001). This choice enables us to obtain abundance patterns that are similar to those obtained with the double degenerate (DD) DTD of Greggio (2005) as well as observationally inferred DTDs (e.g., Totani et al. 2008; Maoz & Graur 2017); for this reason the SD DTD by Matteucci & Recchi (2001) can be considered a good compromise to describe the delayed pollution from the entire SN Ia population. The $R_i(R,t)$ output is also weighted by the initial mass function (IMF). Here we adopt the IMF by Kroupa et al. (1993), which is preferred to reproduce the characteristics of the MW disc (Romano et al. 2005).

The last term in Eq. (1) models the gas infall rate. For the two-infall model, it is computed as

$$\dot{G}_{i,\mathrm{inf}}(R,t) = A(R)\, X_{i,1\mathrm{inf}}(R)\, e^{-\frac{t}{\tau_1}} + \theta(t - t_{\max})\, B(R)\, X_{i,2\mathrm{inf}}(R)\, e^{-\frac{t-t_{\max}}{\tau_2(R)}}, \quad (3)$$

where $G_{i,\mathrm{inf}}(R,t)$ is the infalling material in the form of the element i and $X_{i,J\mathrm{inf}}$ is the infalling gas composition for the Jth infall, assumed to be primordial for the solar annulus; τ_1 and τ_2 are the timescales of the two infall episodes, while $t_{\max}$ indicates the time of maximum infall, which is also the delay between the first and the second infall; the coefficients A and B are set to reproduce the present-day surface mass density of the chemical discs at a certain radius R; and θ is the Heavyside step function.

In the case of the parallel model, since we assume two separate infall episodes, the gas infall law is given instead by two expressions,

$$\dot{G}_{i,\mathrm{thick,inf}}(R,t) = A(R)\, X_{i,\mathrm{thick,inf}}(R)\, e^{-\frac{t}{\tau_1}}, \quad (4)$$

$$\dot{G}_{i,\mathrm{thin,inf}}(R,t) = B(R)\, X_{i,\mathrm{thin,inf}}(R)\, e^{-\frac{t}{\tau_2(R)}}, \quad (5)$$

the first law refers to the high-α formation episode and the second to the low-α formation. Here the different quantities have the same meaning of Eq. (3). In both the chemical evolution scenarios we set $\tau_1 = 0.1$ Gyr and and $\tau_2(8\,\mathrm{kpc}) \simeq 7$ Gyr, in agreement with previous studies (e.g., Grisoni et al. 2017; Spitoni et al. 2019).

During this work, we also ran two-infall and one-infall (i.e. low-α star formation episode of the parallel scenario, see Sect. 4.3) models for the inner and outer radii to test the impact of radial stellar migration. To this end, we adopt the prescriptions described in Palla et al. (2020b) and Grisoni et al. (2018).

In particular, we assume that the disc forms inside-out, meaning that the timescale for mass accretion in the Galactic disc increases linearly with radius (Chiappini et al. 2001; Cescutti et al. 2007):

$$\frac{\tau_2(R)}{\mathrm{Gyr}} \propto \frac{R}{\mathrm{kpc}}. \quad (6)$$

However, the inside-out mechanism is not sufficient to explain the observed trends for present-day radial gradients (both in abundances and in physical quantities, see Palla et al. 2020b). For this reason, a SFE decreasing with radius is adopted (see also Grisoni et al. 2018).

The total surface mass densities for the low-α and high-α disc are assumed to have exponential profiles. For the two discs, we have

$$\frac{\Sigma(R)}{\mathrm{M_\odot\,pc^{-2}}} \propto e^{-R/R_d}, \quad (7)$$

where the disc scale length R_d is 3.5 kpc for the low-α disc (e.g., Spitoni et al. 2017) and 2.3 kpc for the high-α disc (Pouliasis et al. 2017, see also Palla et al. 2020a). This leads to a $\Sigma_{\mathrm{low}}/\Sigma_{\mathrm{high}}$ increasing with radius in agreement with recent observational and theoretical works (e.g., Anders et al. 2014; Spitoni et al. 2021).

For the two-infall model in the inner disc, we also take advantage of the results of Palla et al. (2020b) and Spitoni et al. (2021), suggesting a metal-enriched gas accretion from the second infall episode, as also predicted by some simulations (e.g., Agertz et al. 2021; Renaud et al. 2021a,b).

We note that in both the models we do not include Galactic winds and radial gas flows.

For the winds, it was found that Galactic fountains rather than wind are more likely to occur in galactic discs. Furthermore, there is the indication (e.g., Melioli et al. 2009; Spitoni et al. 2009) that fountains do not alter significantly the chemical evolution of the disc as a whole.

Radial gas flows (e.g., Spitoni & Matteucci 2011) are also neglected in this work, even though they were found to be viable solutions to explain gradients and abundance ratios (e.g., Grisoni et al. 2018; Palla et al. 2020b). Most of the works aimed at studying the solar vicinity assume no flows at all (e.g., Romano et al. 2010; Grisoni et al. 2017; Spitoni et al. 2019). Moreover, tests were performed with radial gas flows, and no substantial differences were found in the general picture.

3.1. Nucleosynthesis prescriptions

The nucleosynthesis prescriptions and the implementation of the stellar yields are fundamental ingredients for chemical evolution models. Massive stars and SNe Ia play a fundamental role in shaping the [Mg/Fe] versus [Fe/H] abundance pattern. Magnesium is mostly produced by massive stars during hydrostatic carbon burning and explosive neon burning (e.g., Woosley & Weaver 1995), whereas SNe Ia are the origin of most of the Fe (e.g., Matteucci 2012), although CC-SNe produce this element in non-negligible amounts. In order to see the effects of the nucleosynthesis prescriptions on the evolution scenarios, we decided to test different stellar yields from the literature. For massive stars we tested the three models described below.

In François et al. (2004; hereafter F04), empirical modification of the solar metallicity yields (Woosley & Weaver 1995) was performed to reproduce the solar Mg abundance. Magnesium yields were increased in the range 11–20 $\mathrm{M_\odot}$ and lowered for stars larger than 20 $\mathrm{M_\odot}$. No modifications were performed for Fe yields computed for solar composition, which do not overestimate Fe abundance as do those of Woosley & Weaver (1995) as functions of metallicity.

The Kobayashi et al. (2006; hereafter K06) SN models use different metallicities where the ^{56}Ni output is calibrated on light curve and spectral fitting of individual SNe. To satisfy this requirement, hypernovae (HNe, i.e. models with explosion energy $E_{\mathrm{SN}} > 10^{51}$ erg) explosions were also computed for $m > 20\,\mathrm{M_\odot}$ in addition to SN models ($E_{\mathrm{SN}} = 10^{51}$ erg). Here we adopt the same set used in Grisoni et al. (2017), where the hypernova fraction (ϵ_{HN}) is set to 1. We note that the K06 table is almost identical for Mg and Fe to those of Kobayashi et al. (2011) and Nomoto et al. (2013).

The Limongi & Chieffi (2018; hereafter L18) SN models use different metallicities where mass loss and stellar rotation are taken into account. In these models the mass cut is chosen in order to allow for the ejection of 0.07 $\mathrm{M_\odot}$ of ^{56}Ni. L18 propose different yield sets for different rotational velocities ($v_{\mathrm{rot}} = 0$, 150, 300 $\mathrm{km\,s^{-1}}$); different minimum mass for failed SNe (i.e. objects fully collapsing to black holes; from 30 $\mathrm{M_\odot}$ to 120 $\mathrm{M_\odot}$); and with or without fallback and mixing process. At variance with F04 and K06 for which the nucleosynthesis computation does not go beyond 40 $\mathrm{M_\odot}$, in L18 yields are computed up to 120 $\mathrm{M_\odot}$. Throughout the paper we only test the effect different rotational velocities and failed SN masses. The mixing and fallback processes do not leave a significant imprint on the analysed abundance patterns.

For SNe Ia we adopt only the yields of the W7 model from Iwamoto et al. (1999). Palla (2021) shows that negligible differences ($\lesssim$0.1 dex) in [α/Fe] ratios are obtained by adopting more

recent (and physical) models for different subclasses of SN Ia explosions (e.g., Seitenzahl et al. 2013; Leung & Nomoto 2020) and that the W7 model can be safely adopted in the analysis of [α/Fe] versus [Fe/H] abundance patterns.

3.2. Implementing stellar radial migration

As mentioned in the Introduction, we include stellar radial migration prescriptions from the literature in the models to test the origin of candidate 'migrators'. We implement migration in the chemical evolution model by adopting two different approaches; one takes the output of hydrodynamical simulations for a MW-like disc, while the other adopts parametric prescriptions. We give the details of the two implementations here.

In the Spitoni et al. (2015; hereafter S15) approach we simply move stars formed at a given radius bin of the model, with a certain age and metal content, to the ring corresponding to the solar annulus (i.e. 8 kpc). To this end, results of the simulations by Minchev et al. (2013) are adopted as a reference. In particular, it is assumed that 10% and 20% of the stars born at 4 and 6 kpc, respectively, migrate towards 8 kpc, while 60% of those born at 8 kpc leave the solar radius. At variance with S15, in this work we also consider that 20% and 10% of stars born at 10 and 12 kpc migrate towards 8 kpc. In the scenario of the two-infall model we also assume that stellar migration has an effect only for the second gas accretion episode since our focus for stellar migration is on the low-α sequence.

In Frankel et al. (2018; hereafter F18) migration is seen as a result of a diffusion process treated in a parametrical way. Following Sanders & Binney (2015) and adapting their parametrisation to a galactocentric radius coordinate, the probability for a star to be currently at a galactocentric radius R_f, given that it was born at R_0 and with age τ, can be written as

$$\ln p(R_f \,|\, R_0, \tau) = \ln(c_3) - \frac{(R_f - R_0)^2}{2\,\sigma_{RM}\,\tau/10\,\mathrm{Gyr}}, \quad (8)$$

where σ_{RM} is the radial migration strength and c_3 a normalisation constant ensuring that stars do not migrate to negative radii (see F18 for details). For σ_{RM} we adopt a value of 3.5, very similar to that found in F18 as a result of their Bayesian fitting procedure. We note that our expression is marginally different from Eq. (10) in F18, where the migration normalisation is set to 8 Gyr. However, we verified that this change does not lead to significant differences in the results. As in the S15 prescriptions, we assume stellar migration for the two-infall model only after the onset of the second infall. It is worth noting that in F18 migration was also not considered for an old disc (age > 8 Gyr in their case) component.

With both the above prescriptions, we assume that radial migration is only a passive tracer of chemical evolution (i.e. the metal enrichment of the ISM in the solar vicinity is practically unaffected by the stars born in other regions). Following Kordopatis et al. (2013), a representative value for the velocity of the migrating stars is 1 km s^{-1}, which roughly corresponds to 1 kpc Gyr^{-1}. Therefore, only stars with stellar lifetimes $\gtrsim$1 Gyr, corresponding to initial masses below 2 $M_\odot$ (see e.g., Fig. 3 of Romano et al. 2005), can travel for distances larger than 1 kpc. Also adopting the parametric approach of F18, the fraction of stars contributing from rings other than that of the solar vicinity is $\lesssim$0.15 for times below 1 Gyr. Therefore, we can reasonably assume that most of the metals produced by a stellar generation are ejected rather close to their progenitor birthplace.

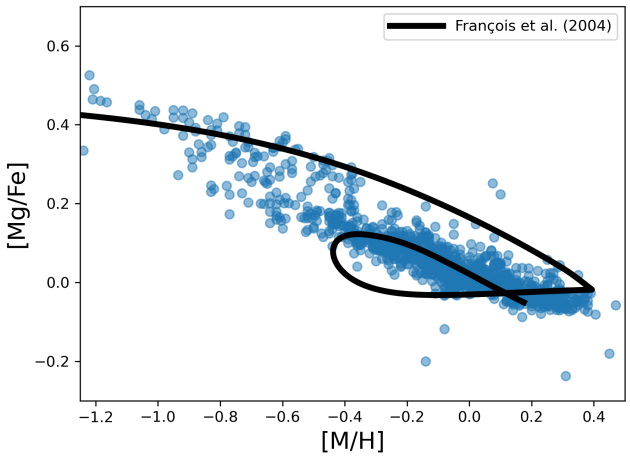

Fig. 3. [Mg/Fe] vs. [M/H] abundance diagram for the delayed two-infall model described in Sect. 3 adopting François et al. (2004) yields for massive stars. The blue points are the data from Santos-Peral et al. (2020, 2021).

4. Results

We ran several models to test the effect of different stellar yields and different scenarios for chemical evolution in comparison with the data from S20 and S21. In particular, we first concentrate on the outcomes of the different nucleosynthesis prescriptions to see the effect of the different yield sets on the predicted abundance ratios. After that we describe the comparison of the two-infall and the parallel model scenarios, with their advantages and disadvantages relative to solar neighbourhood data. Finally, we discuss the possible influence of inner and outer disc stars on the solar vicinity.

4.1. Testing stellar yields

As mentioned in Sect. 3.1, we tested different nucleosynthesis prescriptions for massive stars, whose stellar yields have the largest influence on Mg and Fe evolution.

In Fig. 3 we plot the predicted [Mg/Fe] versus [M/H] by the delayed two-infall model adopting the yields of F04 and compared with the data from S20 and S21. We see that the model reproduces well the data trend for the high-α and the low-α sequence. From a more careful inspection, however, we note that the model fails to reproduce the region occupied by the low-α, low-metallicity stars. This is mainly a consequence of the scenario of chemical evolution.

The observational data are also fairly well reproduced by the same chemical evolution model that adopts the CC-SN yields by K06, as shown in Fig. 4. Nevertheless, we see some differences between Figs. 3 and 4. The Fig. 4 shows a model with slightly enhanced [Mg/Fe] ratios at low metallicities, while at super-solar metallicities a clear underestimation emerges of [Mg/Fe] relative to the trend of the data. This is interesting since S20 highlighted for this dataset a decreasing [Mg/Fe] trend with metallicity, at variance with previous estimates (e.g., Fuhrmann et al. 2017; Mikolaitis et al. 2017). Recalling that the F04 yields are an empirical modification of those of Woosley & Weaver (1995), this discrepancy opens the question of whether CC-SN modelling or abundance determination (despite the optimised derivation procedure) is responsible for this bias. In fact, it is not possible to attribute the deficiency in the predicted [Mg/Fe] to the SN Ia yields, as often suggested in

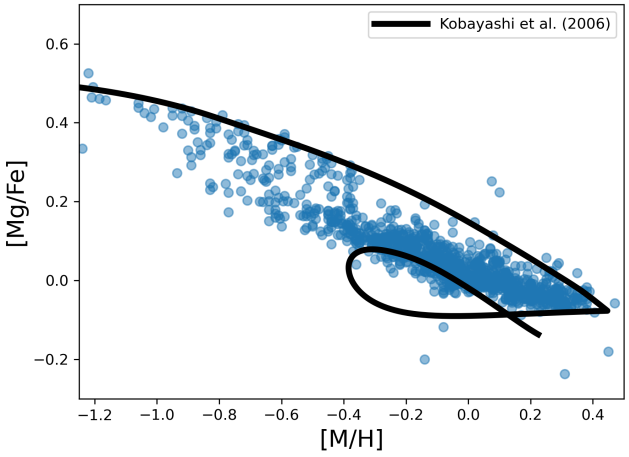

Fig. 4. Same as Fig. 3, but for Kobayashi et al. (2006) yields.

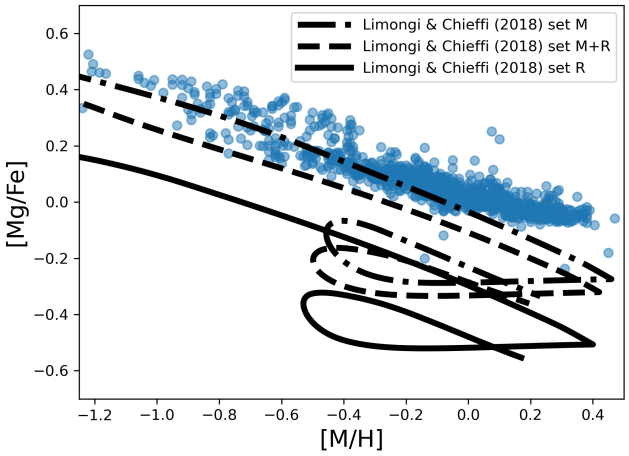

Fig. 5. Same as Fig. 3, but for Limongi & Chieffi (2018) yields. Three sets are shown: solid line for set R with full rotation ($v_{\rm rot}$ = 300 km s^{-1}) up to [Fe/H] = −2, no rotation ($v_{\rm rot}$ = 0 km s^{-1}) afterwards; dashed line for hybrid M+R set (minimum mass for failed SNe > 60 M$_\odot$) with full rotation up to [Fe/H] = −2, no rotation afterwards; dash-dotted line for set M with full rotation at all metallicities.

previous studies (e.g., Magrini et al. 2017; Grisoni et al. 2018). This was clearly shown in Palla (2021), where different SN Ia models were found to have a negligible effect on the [Mg/Fe] ratio.

A completely different picture emerges from Fig. 5. In this figure we show the delayed two-infall model predictions adopting different sets of stellar yields from L18. We note that the L18 set R (solid line) severely underestimate the Mg content at all metallicities by at least 0.2 dex. However, this was expected since Prantzos et al. (2018) already showed that this nucleosynthesis choice does not agree with the obseved behaviour of [Mg/Fe]. This happens even when adopting yields considering stellar rotation, like those shown in Fig. 5. However, the Prantzos et al. (2018) analysis was limited to the set R of L18, for which only stars below 30 M$_\odot$ explode as normal CC-SN, whereas more more massive stars end their lives as failed SNe (see Sect. 3.1). In order to probe the differences found in relaxing this limit and to be consistent with the other yield sets adopted in this paper (where no failed SNe are assumed), we considered other sets from the compilation of L18. In particular, we took a hybrid M+R set, where we assume that only stars above 60 M$_\odot$ directly collapse to a black hole, and the set M, where stars of all masses are considered to die as CC-SNe. Nevertheless, we note that both the hybrid M+R and the M sets (dashed and dash-dotted line, respectively) are not able to explain the observed [Mg/Fe] versus [Fe/H] evolutionary trend. Actually, the model adopting the set M decently reproduces the [Mg/Fe] observed at [M/H] $\lesssim -1$ dex, but it lowers to subsolar values for higher metallicities. This happens even when adopting yields with full rotation ($v_{\rm rot}$ = 300 km s^{-1}) at solar values; in fact, the dependence on the rotation velocity at this metallicity is very modest (see L18).

Because of the very modest agreement between the data from S20 and S21 and the models adopting the different massive star yields from L18, from now on we proceed in our analysis only adopting the sets from F04 and K06.

4.2. Different chemical evolution scenarios

The stellar yields are not the only factor influencing the predicted chemical evolution for the solar neighbourhood. In recent years several different scenarios have been proposed to explain the chemical evolution of the MW disc (e.g., Nidever et al. 2014; Haywood et al. 2016; Grisoni et al. 2017; Spitoni et al. 2019; Sharma et al. 2021). In this section we discuss the results of two different approaches to reproducing the trend observed by S20 and S21: the delayed two-infall model (Spitoni et al. 2019 and later Palla et al. 2020b) and the parallel model (Grisoni et al. 2017, see Sect. 3 for more details).

In Figs. 6 and 7 we show the predicted chemical evolution by the two scenarios proposed above, adopting the two different sets of stellar yields selected in Sect. 4.1. It is worth noting that in order to compare the predictions of the models with observations, we took the selection function of the observational data (see Sect. 2) into account. Since this function is age and metal dependent, because the fraction of stars within the selection window changes with the age and metallicity, we include in our models a selection fraction $f(\tau, [{\rm M/H}])$ computed as

$$f(\tau, [{\rm M/H}]) = \frac{\int_{M_a(\tau,[{\rm M/H}])}^{M_b(\tau,[{\rm M/H}])} \phi(m)\,{\rm d}m}{\int_{M_{\rm min}}^{M_{\rm max}(\tau)} \phi(m)\,{\rm d}m}, \quad (9)$$

where $\phi(m)$ is the IMF and M_a and M_b are the initial masses of the stars that are in the M_J, log(g), and $T_{\rm eff}$ ranges for a population of age τ and metallicity [M/H]. To do this, we adopt PARSEC (release v1.2s) and COLIBRI (release S37) stellar evolutionary tracks (Bressan et al. 2012; Chen et al. 2014, 2015; Tang et al. 2014; Marigo et al. 2017; Pastorelli et al. 2019, 2020) for selecting the range of masses in the selection window at different ages and metallicities computed by the chemical evolution model.

Figure 6 shows that both the F04 (upper panel) and K06 (lower panel) stellar yields reproduce the trends of the high-α and the low-α sequences defined in Sect. 2. The model also predicts well the bulk of the stellar distribution in the [Mg/Fe] versus [M/H] plane. Especially in the case adopting F04 yields, the peak in the stellar counts (see Fig. 6 colour bar) coincides with the densest data region of the diagram (magenta contours). However, it can be seen that the two models do not explain the low-α, low-metallicity ([M/H] $\lesssim -0.6$ dex) data or the high-metallicity tail (above [M/H] ~ 0.2 dex) of the low-α sequence. Even if the models cover the high-metallicity region at the end of the first infall, the number of stars predicted by the simulation at that point is negligible. This is evident by looking at the Fig. 6 colour bar.

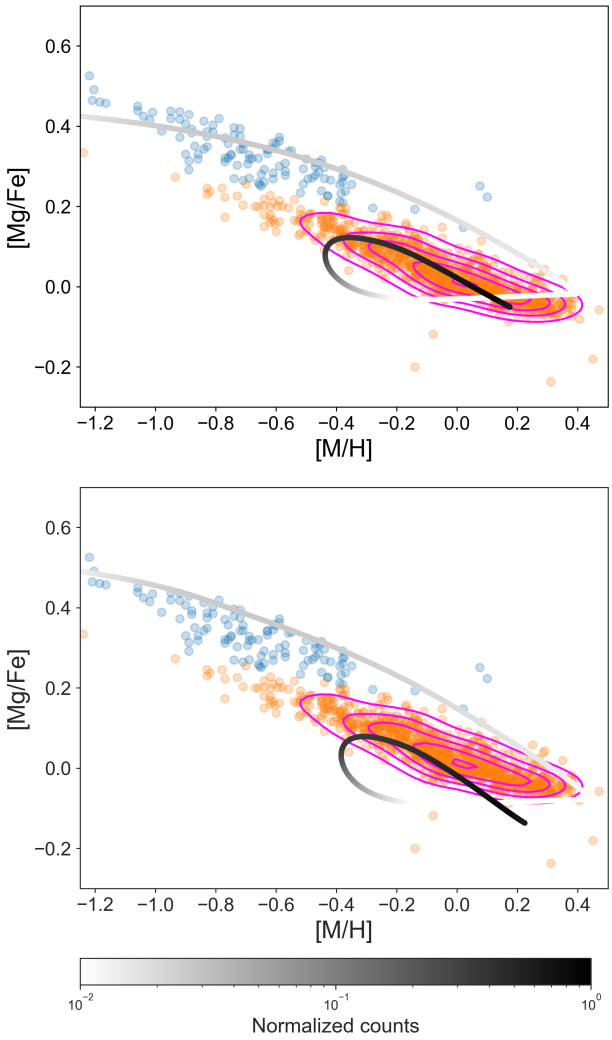

Fig. 6. [Mg/Fe] vs. [M/H] abundance diagram for the delayed two-infall model scenario of chemical evolution with François et al. (2004) yields (*upper panel*) and Kobayashi et al. (2006) yields (*lower panel*). The colour bar indicates the predicted stellar number counts (normalised to the maximum value) at a certain point of the diagram, taking into account the selection function. The light blue points are the observed high-α stars, whereas the orange points are the observed low-α stars. The magenta contour lines enclose the observed density distribution of stars.

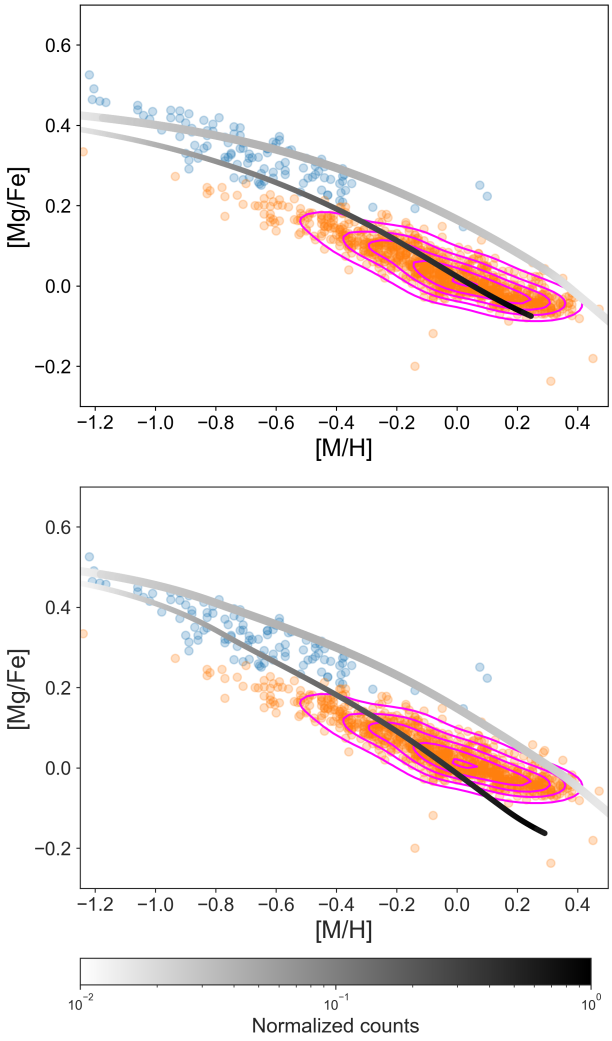

Fig. 7. Same as Fig. 6, but for the parallel model scenario of chemical evolution. The thin lines represent the chemical track for the low-α star formation episode, whereas the thin lines are the chemical track for the high-α star formation episode.

As noted in Sect. 4.1, the two-infall model with the K06 yields (Fig. 6 lower panel) also underestimates the [Mg/Fe] values at high metallicity. This happens in spite of the results of S20, who obtained a decreasing trend in the [Mg/Fe] data even at supersolar metallicity, differently from previous estimates (e.g., Fuhrmann et al. 2017; Mikolaitis et al. 2017).

In Fig. 7 we show the results for the parallel model adopting the yields of F04 (upper panel) and K06 (lower panel). By looking at the chemical tracks for the high-α star formation episode (thick lines), we note that this sequence explains well the stellar distribution observed for the high-α stars with both the nucleosynthesis prescriptions adopted. At variance with the delayed two-infall model, we see that the parallel scenario helps to explain the scatter observed for the high-α stars. Similarly to Fig. 6 with the two-infall model, the parallel scenario in Fig. 7 has problems in explaining the low-metallicity ([M/H] $\lesssim -0.6$ dex) low-α stars. Moreover, in the upper and lower panels we see that the thick disc model curve can explain only a minimal part of the highest metallicity ([M/H] $\gtrsim 0.2$ dex) stars, due to the very low stellar density predicted by the model (see Fig. 7 colour bar). Nonetheless, the parallel scenario is able to explain the bulk of observed stars by S20 and S21 (magenta contours) adopting the stellar yields of either F04 or K06.

However, with the latter yield set (Fig. 7 lower panel), it is evident that the model for the thin disc underestimates the predicted [Mg/Fe] at supersolar metallicity. The same feature is visible for the two-infall scenario when we adopt the prescriptions of K06. This confirms even more that the high-metallicity subsolar Mg obtained with the K06 set is a yield-dependent feature that does not depend on the adopted chemical evolution scenario.

Considering stellar ages In order to probe the scenarios of chemical evolution on firmer bases, we decided to compare our models with the subsample of MSTO stars (see Sect. 2) for which accurate stellar ages were derived. The further dimension available for this subsample provides an important test for the two scenarios of chemical evolution, highlighting features that are hidden when looking at the abundance diagrams only.

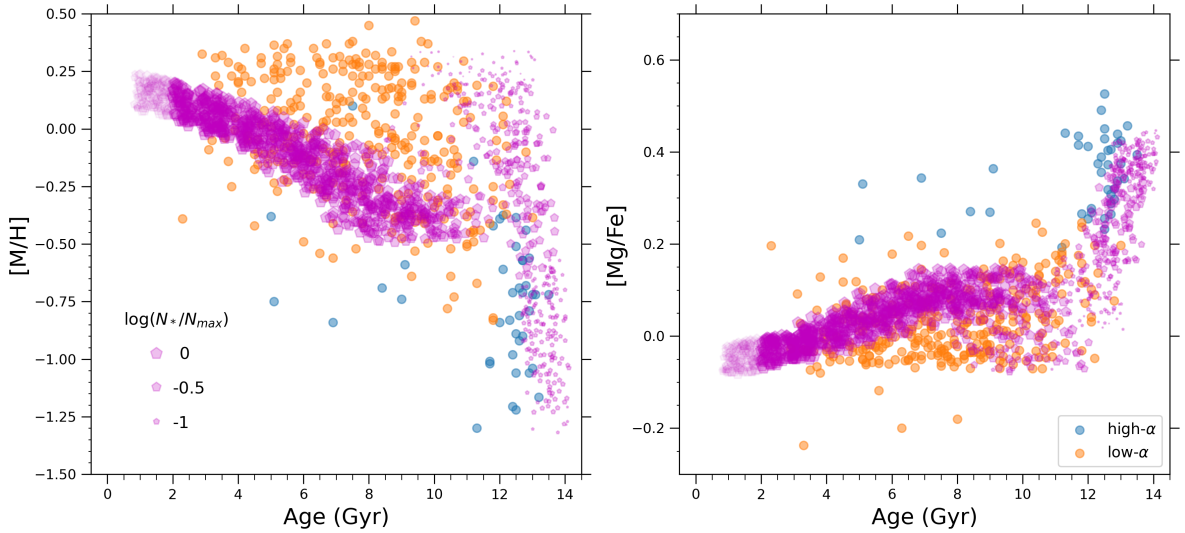

Fig. 8. Synthetic model results for the time evolution of [M/H] (*left panel*) and [Mg/Fe] (*right panel*) distributions produced by the delayed two-infall model in combination with the age and abundance uncertainties of the MSTO subsample (see Eqs. (10)–(12)). The stellar yields are from François et al. (2004). Purple filled pentagons are the mock data from the synthetic model. The pentagon size indicates the local number density of formed stars normalised to maximum value, taking into account the selection function. Pentagons with age below 2 Gyr are shaded due to the absence of stellar data in this region. The light blue points are the observed high-α stars, whereas the orange points are the observed low-α stars of the MSTO subsample.

To avoid biased conclusions in the comparison, we selected the predicted stars according to the selection function for the MSTO subsample (see S21 for details). Moreover, we took into account the uncertainties in stellar age and abundance determinations by building a synthetic chemical evolution model (i.e. a mock stellar catalogue of surviving stars). Similarly to the procedure adopted in Spitoni et al. (2019), we added at each Galactic time a random error to the ages and the abundances of the stars formed at the Galactic time t. The random errors are uniformly distributed in the interval of the average error estimated for a certain abundance and time. In this way, for the synthetic model, we have a new age, defined as

$$\tau_{\rm new}(t) = \tau(t) + U([-\sigma_{\tau(t)}, +\sigma_{\tau(t)}]), \quad (10)$$

where $\tau(t) = (13.7 - t)$ Gyr, U is the random function with uniform distribution, and $\sigma_{\tau(t)}$ is the average error in the age determination at the time t. This value ranges from ∼0.25 to ∼2 Gyr. In parallel, we implement the error on the metallicity [M/H] to define a new metallicity,

$$[{\rm M/H}]_{\rm new}(t) = [{\rm M/H}](t) + U([-\sigma_{\rm [M/H]}, +\sigma_{\rm [M/H]}]), \quad (11)$$

where $\sigma_{\rm [M/H]}$ is independent of age and metallicity and has a value of 0.08 dex. The same is done for [Mg/Fe], for which we define

$$[{\rm Mg/Fe}]_{\rm new}(t, [{\rm Mg/Fe}]) = [{\rm Mg/Fe}](t) + U([-\sigma_{\rm [Mg/Fe]([Mg/Fe])}, +\sigma_{\rm [Mg/Fe]([Mg/Fe])}]). \quad (12)$$

In this case, $\sigma_{\rm [Mg/Fe]([Mg/Fe])}$ is the average error in a [Mg/Fe] bin, with typical values of the order of 0.02–0.03 dex (see Sect. 2).

In Fig. 8 the results of the time evolution of [M/H] (left panel) and [Mg/Fe] (right panel) ratios including the errors described in Eqs. (10)–(12) are reported for the delayed two-infall model. To avoid confusion, from now on we plot only the results obtained using F04 yields, which best explain the S20 and S21 abundance data. However, we find similar conclusions even when the K06 prescriptions are adopted.

The analysis of Fig. 8 confirms the problems of the two-infall model already found in Fig. 6. The model fails to reproduce a few of the low-α low-metallicity stars, but mostly does not predict the stars with the highest metallicity. This is evident in Fig. 8 left panel, where we also note that these high-metallicity stars (hereafter super metal-rich, SMR, stars [M/H] $\gtrsim 0.1$ dex) have a large spread in stellar ages from 10 Gyr to the most recent ages in the sample (∼2 Gyr). This spread can be hardly accounted for in a scenario of homogeneous chemical evolution in a single disc zone, even accounting for observational errors. Moreover, we do note expect a large intrinsic scatter for stars of the same age and birthplace (see e.g., Ness et al. 2019; Sharma et al. 2022), hence we can attribute this spread to outward radial migration for a fraction of stars of the MSTO sample. This idea is also supported by the right panel, where quite a large scatter (∼0.2 dex) is seen for [Mg/Fe] for $\tau < 10$ Gyr. In this case the model does not reproduce well the low-[Mg/Fe] stars with intermediate ages, which correspond to the high-metallicity stars in that age range.

In the two panels of Fig. 8 we also note that some classified high-α stars (blue points) show very young ages in contrast to the majority of the objects of this class, which show $\tau > 10$ Gyr. These can be considered young α-rich (YαR) stars, whose origin is still debated and attributed either to stars migrated from the Galactic bar (e.g., Chiappini et al. 2015) or more probably evolved blue stragglers (e.g., Martig et al. 2015; Yong et al. 2016; Jofré et al. 2016; Izzard et al. 2018; Zhang et al. 2021).

In Fig. 9 we show again the time evolution of [M/H] (left panel) and [Mg/Fe] (right panel) ratios including the errors described in Eqs. (10)–(12), but for the parallel scenario of chemical evolution. In the left panel of Fig. 9, we observe that the general scenario is similar to that of the two-infall model. The model fails to reproduce the observed low-metallicity intermediate-young stars as well as most of the SMR stars. However, it is clear that this scenario has more problems in predicting the low-metallicity stars relative to the two-infall model in Fig. 8. On the contrary, the parallel model has fewer problems on

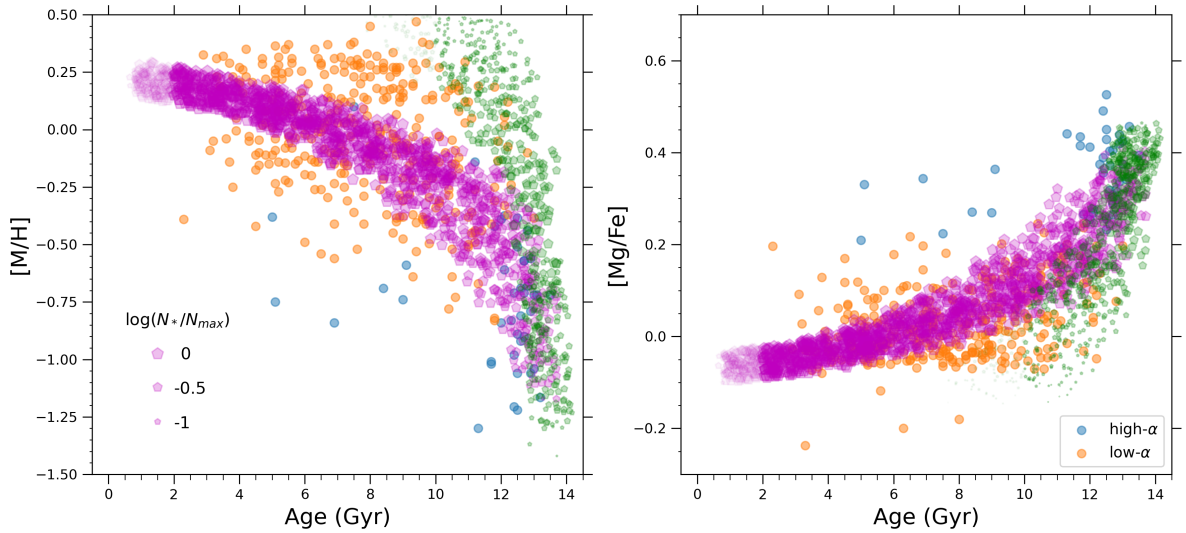

Fig. 9. Same as Fig. 8, but for the parallel model. The adopted yields are from François et al. (2004). Green filled pentagons are the mock data of the high-α sequence of the synthetic model, whereas purple filled pentagons indicate the mock data of the model low-α sequence. In the former case, the pentagons are shaded if the age is below 10 Gyr and the contribution to the total stellar density of younger stars is negligible.

the side of intermediate-young high-metallicity stars. This difference between the parallel and the two-infall scenarios is mostly caused by the higher metallicities reached by the evolutionary track with lower α values than by the second infall episode at similar ages. As can be seen in Fig. 9, the high-α track does not help much in reproducing high-metallicity stars. The pentagon sizes in Fig. 9 (the predicted number of stars after the first Gyr of evolution) appear to be too small, as already noted in Fig. 7.

In the right panel of Fig. 9, we see that the spread in [Mg/Fe] is hardly reproduced, also in the case of the parallel model. At variance with the two-infall scenario, the lower α track sequence predicts lower [Mg/Fe]; as in Fig. 9 left panel, this can be attributed in part to the higher metal enrichment at similar age of this scenario (see Matteucci 2003, 2012). However, the model still struggles to reproduce the lowest [Mg/Fe] data at intermediate ages.

The analysis of the sample of the MSTO stars including stellar age estimates seems to indicate that a fraction of these stars have experienced a radial migration from the place of birth.

Even though the MSTO subsample is not complete, the indications coming from Figs. 8 and 9 are quite evident. In particular, it seems from this analysis that most of the observed SMR (and lowest [Mg/Fe]) stars observed in the solar vicinity should have formed in faster chemically evolving environment, such as that of the inner disc (see also Minchev et al. 2013; Kordopatis et al. 2015). This suggestion is also supported by looking at the stellar specific angular momentum behaviour with metallicity in the sample of S20 and S21. We observe that the mean angular momentum for SMR stars is anti-correlated with [M/H]; this is a clear consequence of radial migration from the innermost regions of the disc (see also Sharma et al. 2021). The mean angular momentum increases with radius because $J_\phi = v_{\rm circ} R$; therefore, the lower the radius, the lower the angular momentum.

4.3. Impact of inner and outer disc on the solar neighbourhood

The difficulties encountered by both the chemical evolution scenarios in predicting low-α low-metallicity stars and SMR stars (see Sect. 4.2) point towards a context where these stars were born at different Galactic locations from the solar vicinity.

In this section we test the origin of these stars in the light of the scenarios of chemical evolution described in Section 3. First, we take advantage of the works of Grisoni et al. (2018) and Palla et al. (2020b) (see also Spitoni et al. 2021), which proposed parametrisations for different galactocentric radii within the framework of the one-infall model[4] and the delayed two-infall model. Having tested if these chemical pathways are viable to describe the low- and high-metallicity tails of the low-α sequence, we implemented stellar radial migration prescriptions (Spitoni et al. 2015; Frankel et al. 2018, see Sect. 3.2) to probe the proposed scenarios.

In Fig. 10, we show the results of two-infall and one-infall models for outer ($R > 9$ kpc) galactocentric radii. As can be seen in the upper panel, the standard two-infall model for outer Galactic regions (thick dash-dotted line) enables us to reproduce only part of the low-α low-metallicity data (red points). To recover a good agreement between the two-infall model and the bulk of low-α metal-poor stars, we need to adopt a higher ratio between the low-α present-day surface mass density ($\Sigma_{\rm low}$) and the high-α density ($\Sigma_{\rm high}$). Adopting a higher ratio of surface mass densities ensures that lower metallicities are reached during the second infall episode because of the larger proportion of pristine gas, which favours the presence of a more prominent loop feature (see Spitoni et al. 2019). For this reason, we ran a model where we increased $\Sigma_{\rm low}/\Sigma_{\rm high}$ by a factor of 3 (thin dash-dotted line), leaving the other prescriptions unchanged. Despite the ad hoc prescription, this model is physically motivated by the observations coming from large surveys at large galactocentric radii (e.g., Queiroz et al. 2020).

In the lower panel instead, we see that the one-infall model for outer radii naturally reproduces the tail of the low-α data distribution. To test the reliability of this solution even more, in Fig. 10 we highlight the stars from S20 and S21 with guiding radius R_g larger than 9 kpc (yellow crosses). These stars are found in the solar neighbourhood thanks to their quite eccentric orbits, and thus are ideal candidates for being blurred stars from the outer regions. As can be seen in Fig. 10 lower panel,

[4] In this section we do not consider the parallel scenario, but rather the one-infall model. This model traces the formation of the low-α sequence alone.

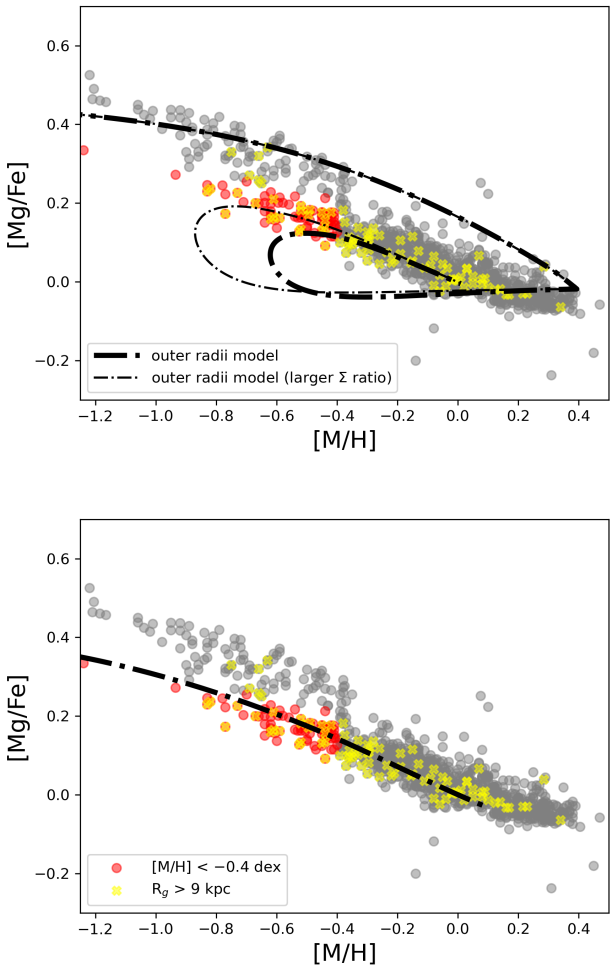

Fig. 10. [Mg/Fe] vs. [M/H] abundance diagram for the delayed two-infall (*upper panel*) and the one-infall (*lower panel*) models for outer galactocentric radii (R = 12 kpc, dash-dotted lines). The stellar yields are from François et al. (2004). The red points are the observed low-α low-metallicity stars ([M/H] < −0.4 dex), whereas the yellow crosses indicate the stars with guiding radius (R_g) larger than 9 kpc.

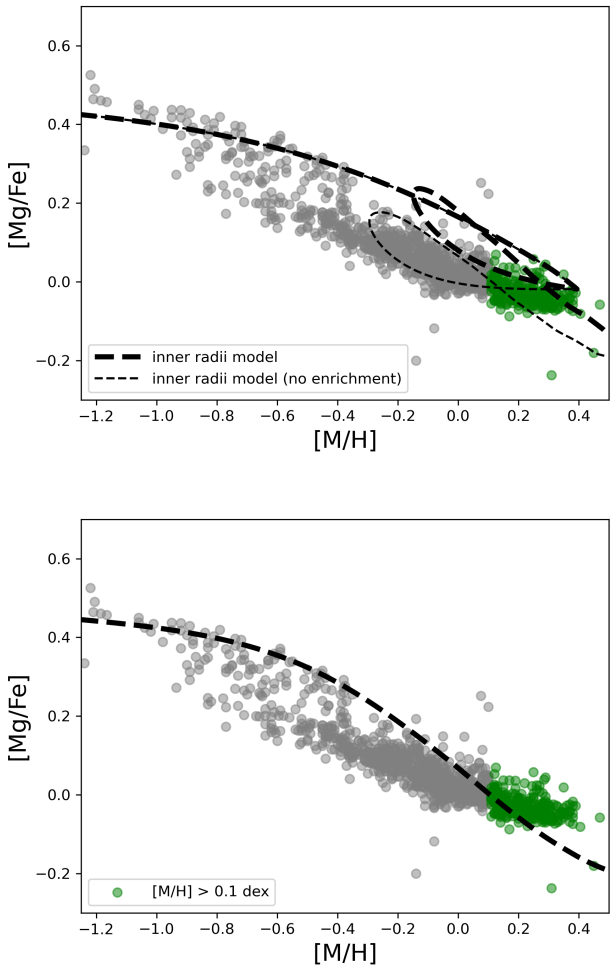

Fig. 11. Same as Fig. 10, but for models for inner galactocentric radii (R = 4 kpc, dashed lines). The stellar yields are from François et al. (2004). Green points indicate the observed SMR stars ([M/H] > 0.1 dex).

the one-infall model for outer galactocentric radii reproduces the abundance trend for most of the data with large R_g.

In Fig. 11, we do the same as in Fig. 10, but for the two-infall and one-infall models for the inner (R < 7 kpc) regions of the disc. In order to highlight the region where the model for the solar neighbourhood struggles to reproduce the data, we plot in green the observed SMR stars. In Fig. 11 upper panel, we show the chemical tracks obtained with the two-infall model for inner radii. In particular, we display a model without second infall pre-enrichment (thin dashed line) and a model with the second infall enriched at [Fe/H] = −0.75 dex level (thick dashed line). It is worth noting that metal-enriched gas accretion was suggested by Palla et al. (2020b) and Spitoni et al. (2021) to explain the APOGEE data (Hayden et al. 2015; Ahumada et al. 2020) for the inner regions of the MW disc. They argue that this infall enrichment could originate from the formation of the thick disc, Galactic halo, Galactic bar, or previous merger events, which then gets mixed with a larger amount of infalling primordial gas, as also suggested by several cosmological simulations (Renaud et al. 2021b; Khoperskov et al. 2021).

The chemical track of the model with enrichment in the second gas accretion episode better reproduces the bulk of the SMR stars as the enrichment in the second infall enables a larger increase in [α/Fe] (see also Palla et al. 2020b). Without any pre-enrichment, the model tends to predict a value of [α/Fe] that is a bit too low for a given metallicity.

In Fig. 11 lower panel we note that the one-infall model has similar problems to the two-infall model without infall pre-enrichment. The predicted [Mg/Fe] for [M/H] $\gtrsim$ 0.2 dex are generally lower than that observed for SMR stars.

4.3.1. Considering stellar radial migration

To make a step forward in our analysis, the chemical tracks described in this section are implemented with detailed prescriptions for stellar radial migration (S15, F18). It is worth noting that similar results are found when adopting these two prescriptions for both the two-infall (Fig. 12) and the one-infall (Fig. 13) scenarios. For this reason, we decided to show only the results obtained with the most recent F18 prescriptions.

In Figs. 12 and 13 we show the evolution of [Mg/Fe] versus [M/H] considering radial migration effects at different age bins. This plot can deliver fundamental information about stars in our sample. We need to fit both abundance and age data simultaneously by adopting the MSTO subsample by S21. To obtain a fair comparison with the data, the stellar selection function and

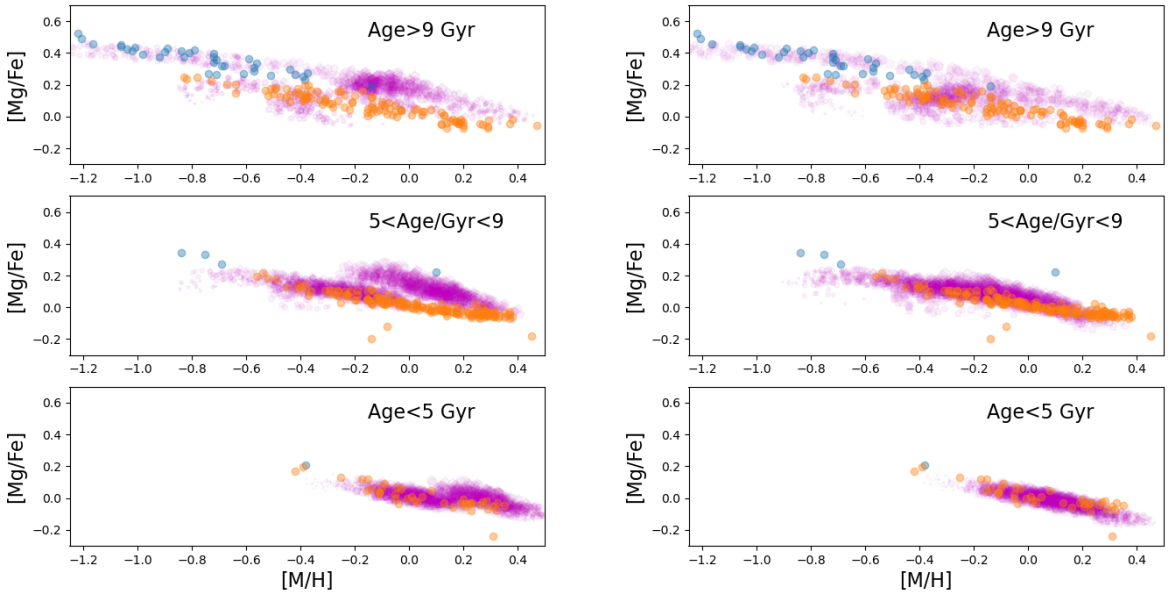

Fig. 12. Synthetic model results for [Mg/Fe] vs. [M/H] distributions including stellar migration produced by the delayed two-infall model with second infall enrichment for inner radii (*left panels*) and without second infall enrichment (*right panels*). The radial migration prescriptions are from Frankel et al. (2018). The stellar yields are from François et al. (2004). Purple filled pentagons are the mock data from the synthetic model. Mock and observational data for the MSTO subsample are plotted as in Fig. 8, with density normalisation done independently for each panel. *Upper panels*: stars older than 9 Gyr. *Middle panels*: stars with ages between 9 and 5 Gyr. *Bottom panels*: Stars younger than 5 Gyr.

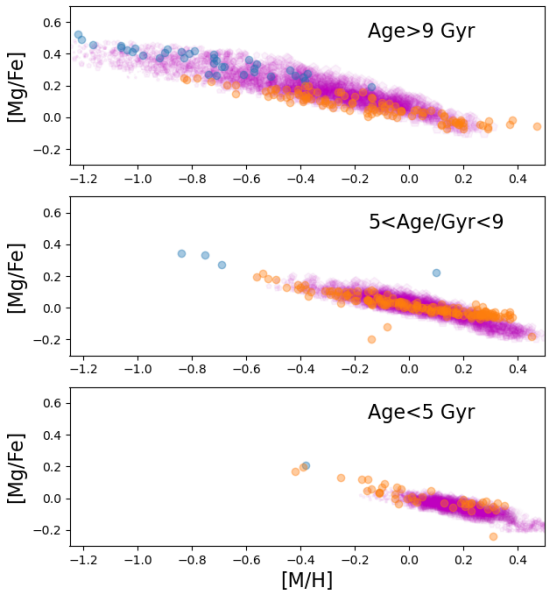

Fig. 13. Same as Fig. 12, but for the one-infall model. The stellar yields are from François et al. (2004). Radial migration prescriptions are from Frankel et al. (2018).

observational errors are taken into account in the models, as in Sect. 4.2.

In Fig. 12 left panels we show the results for the two-infall model adopting a second infall pre-enrichement for $R < 7$ kpc. It is evident that this assumption causes the presence of a large number of high-α stars at high metallicity, which are not observed in the MSTO subsample nor in the total sample by S20 and S21. The problem does not hold anymore if we do not assume an enrichment in the second gas accretion (Fig. 12 right panels), with all the predicted stars lying in the low-α sequence in the two most recent age bins. However, it is worth noting that in the oldest age bin, this model has problems in predicting the low-α SMR stars, even considering the observational uncertainties.

On the other hand, the model is able to reproduce the low-metallicity tail of low-α stars at different age bins. This is possible thanks to the increased ratio of low-α to high-α surface mass density, which favours the presence of a more prominent loop feature at the start of the second infall episode and so the presence of more metal-poor stars.

For the one-infall model in Fig. 13 we see that the mock data reproduce the bulk of MSTO stars in all age bins. We also note that although we take into account stellar migration from the inner and outer regions, the model still struggles to reproduce the low-metallicity tail of the low-α sequence, especially in the young and intermediate-age bins.

The [M/H] and [Mg/Fe] distribution functions for the two-infall and one-infall models are shown in Figs. 14 and 15, respectively. In addition to the global distribution function (which take into account the observational uncertainties), in each panel we show the contribution from the stars born at different galactocentric radii bins.

Starting from the two-infall model (assuming no enrichment in the second infall for the inner radii), we see that the overall [M/H] distribution (Fig. 14 top panel) is well reproduced: the peak in the model distribution coincides with that from the data and no lack of stars at high [M/H] is observed. However, a partial deficiency of the low-metallicity tail contribution is still seen for the two-infall model. This can be solved by assuming more stars migrated from outer radii or by adopting a higher $\Sigma_{\rm low}$ in the outer regions of the disc, which corresponds to a flatter density profile for the low-α population in the outer radii. This last solution can be also seen in the context of the higher $\Sigma_{low}/\Sigma_{\rm high}$ ratio needed to reproduce the low-α low-metallicity data, providing an alternative explanation to that of a suppressed high-α population density in the outermost disc.

The [Mg/Fe] distribution function (Fig. 14 bottom panel) is also well reproduced by the two-infall model, with the peak of

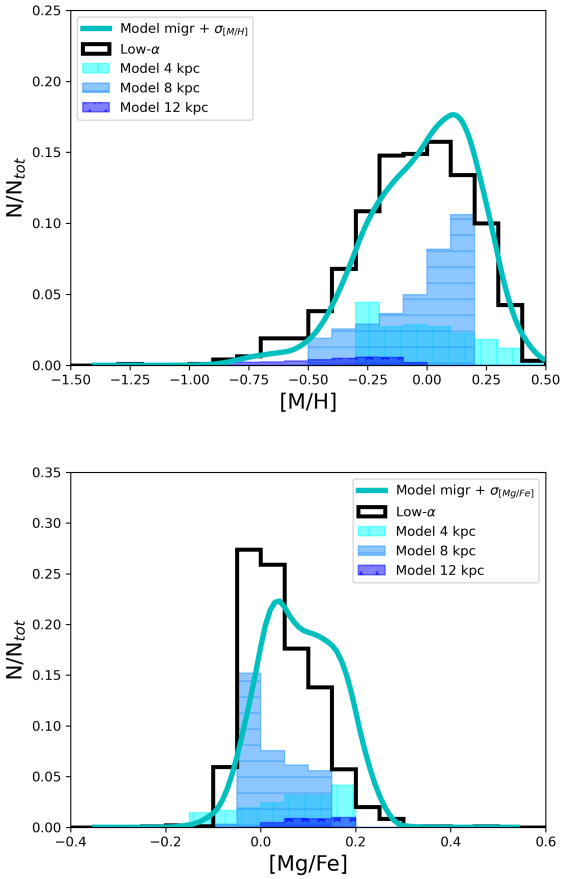

Fig. 14. [M/H] and [Mg/Fe] distribution functions observed for low-α stars (black histogram) compared with the theoretical distribution functions for the two-infall model including migration prescriptions from Frankel et al. (2018) (cyan line) and corrected for the selection function. The theoretical distribution functions are convoluted with Gaussians with $\sigma_{[M/H]}$ and $\sigma_{[Mg/Fe]}$ (see Sect. 4.2). The cyan, light blue, and blue shaded regions indicate the contribution from stars born around 4 kpc, 8 kpc, and 12 kpc, respectively.

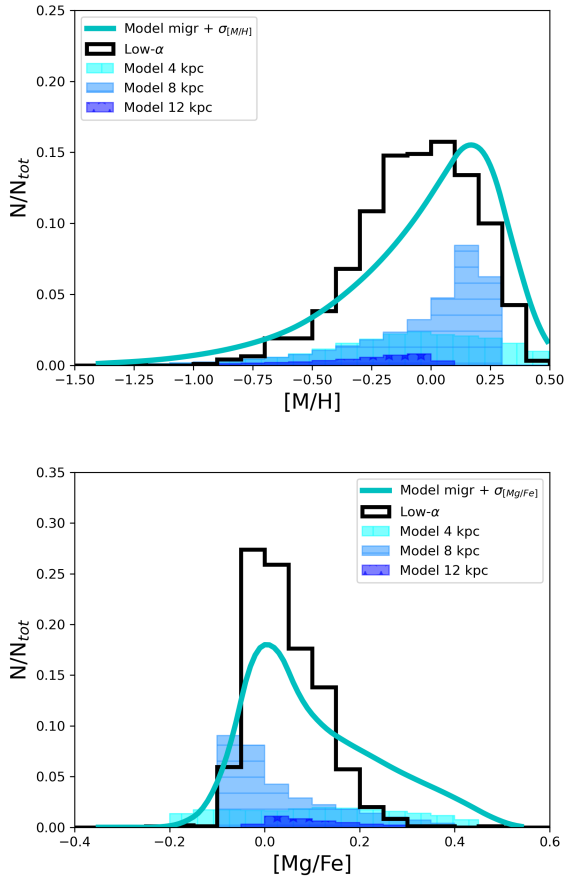

Fig. 15. Same as Fig. 14, but for the one-infall model. The stellar yields are from François et al. (2004). The radial migration prescriptions are from Frankel et al. (2018).

the model distribution that coincides with that of the data. In this case we note a slight overabundance of low-Mg stars relative to the sample of S20 and S21. This is due to the contribution of the stars from the innermost radii, as we can see from Fig. 14 bottom panel (see also Fig. 11). This happens even though we adopted the F04 yield set, which was the only one that does not predict a consistent [Mg/Fe] underestimation at high metallicity (see Sects. 4.1 and 4.2).

For the one-infall model in Fig. 15, we see that the scenario reproduces quite well the observed [M/H] distribution (Fig. 15 top panel). However, the predicted peak is shifted towards higher metallicities, and the situation does not change even when we consider less efficient radial migration. The 8 kpc bin has a peak in the distribution function at values similar to those shown in Fig. 15.

However, larger problems are seen in the [Mg/Fe] distribution function (Fig. 15 bottom panel). In particular, the one-infall model predicts too many stars with high Mg. This is the consequence of having a model with primordial gas accretion.

Therefore, we can say that the two-infall model is the best to reproduce the observed low-α stellar distribution in S20 and S21. Moreover, the predicted [Mg/Fe] distribution function by the one-infall scenario points towards an overestimation of the high [Mg/Fe] stars even including the high-α data of S20 and S21 (which should already be explained by the other model sequence).

In Fig. 16 we show the impact of radial migration in shaping the distribution functions. In particular, we show the results obtained with the two-infall model; however, we can make similar considerations if we plot the results for the one-infall model.

What we note is that, overall, the predicted stellar distributions are not substantially affected by migration. In particular, the positions of the peaks are left roughly unchanged and the same happens if we look at the predicted median [M/H] and [Mg/Fe] ratios (see vertical dashed lines).

However, radial migration is needed to improve the agreement between model predictions and observations. In particular, this is necessary to explain the low- and high-metallicity tails of the [M/H] distribution, even if it is worth remembering that the high [M/H] may be biased towards higher values due to sample selection effects of the usual log g, $T_{\rm eff}$ cuts (see S21).

Nevertheless, from Fig. 16 it is evident that the stellar distribution functions cannot be used to extract information on the extent and significance of stellar migration. For this reason, it is very hard to quantify the impact of stellar radial migration in the sample by S20 and S21.

The need for models describing the evolution at different galactocentric radii to explain the trends of the data confirms that radial migration actually plays a role in shaping the abundance observed in the solar neighbourhood, but the information we can extract from the previous figures cannot say much about the

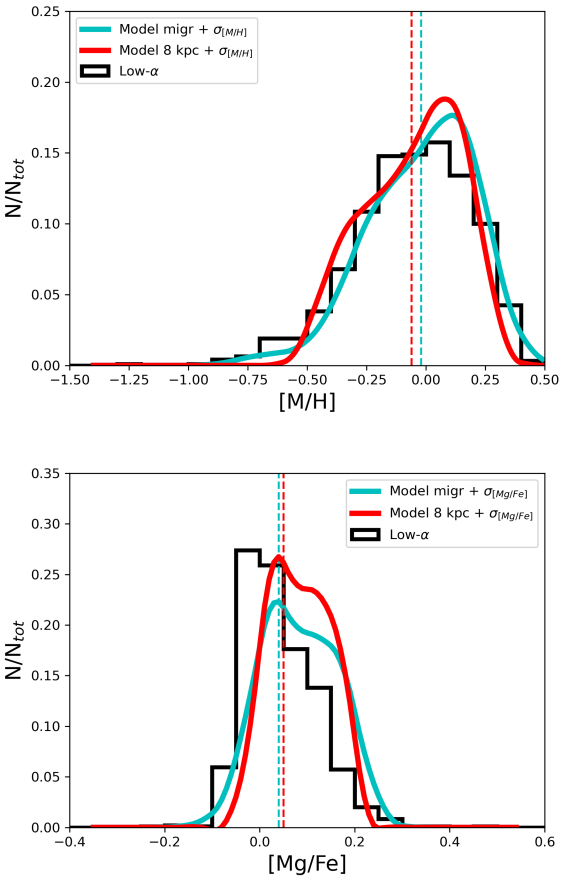

Fig. 16. [M/H] and [Mg/Fe] distribution functions observed for low-α stars (black histogram) compared with the theoretical functions for the two-infall model including migration prescriptions from Frankel et al. (2018) (cyan line) and no migration (red lines). The vertical dashed lines are the median [X/Y] ratios for models with migration (cyan) and without (red).

fractional contribution from stars born outside the solar vicinity. The migration prescriptions adopted in this subsection predict between 50% and 30% of the stars observed born in the solar neighbourhood, but the results about the [Mg/Fe] versus [M/H] evolution and the distribution functions are rather similar.

5. Discussion and conclusions

In this paper we have compared the new [Mg/Fe] abundance measurements by Santos-Peral et al. (2020, 2021) with detailed chemical evolution models for the solar vicinity, exploring different stellar yields (François et al. 2004; Kobayashi et al. 2006; Limongi & Chieffi 2018) and chemical evolution scenarios (delayed two-infall, e.g., Palla et al. 2020b, and parallel, e.g., Grisoni et al. 2017). In the light of the obtained results, we also consider the possible impact of stellar radial migration on the adopted sample by implementing migration prescriptions from the literature (Spitoni et al. 2015; Frankel et al. 2018).

In Santos-Peral et al. (2020) an optimised normalisation procedure was performed for the high-resolution stellar spectra obtained by HARPS in the context of the AMBRE project (de Laverny et al. 2013). The new procedure allows a significant improvement in the abundance determination precision, showing a decreasing trend in [Mg/Fe] with metallicity at high metallicity, at variance with previous works (e.g., Adibekyan et al. 2012; Hayden et al. 2017). In this way it is possible to test whether the discrepancy between the observed flat trend in the metal-rich disc and the steeper slope predicted by the models can be solved by these abundance measurements. The value of this dataset was even enhanced in Santos-Peral et al. (2021), in which reliable stellar age estimates were presented for a subsample of MSTO stars. All the Santos-Peral et al. (2020, 2021) data are cross-matched with the *Gaia* DR2 catalogue (Gaia Collaboration 2018) in order to extract the main kinematical and dynamical stellar parameters.

The comparison between the wealth of chemical, age, and orbital information has allowed us to place constraints not only on the Mg stellar production by stellar sources and on the evolutionary scenarios describing the solar vicinity, but also to describe the influence of stellar migration within a few hundred parsecs of the Sun. In this way we also test which histories of chemical evolution the inner and outer Galactic regions should have experienced. The main results of this work can be summarised as follows:

1. The adoption of different sets of massive star stellar yields have a crucial impact on the predicted chemical evolution. To recover a good agreement with Santos-Peral et al. (2020, 2021) data, we have still to rely on the semi-empirical yields by François et al. (2004). Acceptable results are still obtained using the Kobayashi et al. (2006) yield set, even though a steeper [Mg/Fe] trend at high metallicity is predicted relative to the new abundance data, claiming either a revision of CC-SN yields or further biases in the abundance determination (despite the optimised derivation shown in Santos-Peral et al. 2020). Instead, the various nucleosynthesis results proposed by Limongi & Chieffi (2018) have severe problems in recovering the observed [Mg/Fe] both at low and high metallicity, even adopting the most Mg-rich yield sets. The robustness of these results relative to model parameter variations suggests that we should take with caution the choice of the yield set when dealing with Mg and that further work must be done in the context of the stellar nucleosynthesis for this element;
2. Both the delayed two-infall and the parallel scenarios of chemical evolution satisfactorily reproduce the bulk of the Santos-Peral et al. (2020, 2021) data in the [Mg/Fe] versus [M/H] plane for both the high-α and the low-α sequences. However, they both encounter problems in explaining the metal-rich tail of the data ([M/H] $\gtrsim$ 0.1–0.2 dex) as well as the most metal-poor stars of the low-α sequence. In order to test these results on firmer bases, we compare our models to the Santos-Peral et al. (2021) MSTO subsample with stellar ages. Even applying an a posteriori error on the chemical evolution tracks (see Sect. 4.2), the models struggle to reproduce the metal-rich and metal-poor tails of the low-α sequence, indicating that these stars have experienced radial migration from their original birthplace;
3. We tested the origin of the migrated stars in the light of the one-infall and delayed two-infall scenarios by taking advantage of the prescriptions by Grisoni et al. (2018) and Palla et al. (2020b) for inner and outer disc chemical tracks. We find that low-α, low-metallicity stars are likely to be outer disc candidates. These stars are well explained by a two-infall model with prescription suited for the outer disc (e.g., longer infall timescale due to inside-out, reduced star formation efficiency) and with negligible high-α population surface mass density at large galactocentric distances. In particular, this latter feature can be seen in the context of the lack outer disc stellar data by large surveys

(e.g., Queiroz et al. 2020). However, we cannot exclude higher low-α population surface densities than those predicted for the outer disc to be the cause of this behaviour. At the high-metallicity end of the low-α sequence, we can explain these stars in terms of stars migrated from the inner disc. At variance with previous works (e.g., Palla et al. 2020b), we exclude that inner disc regions are formed by an enriched gas accretion episode. However, it is worth remembering that different datasets and stellar yields prescriptions were adopted in these previous papers. We also find that the one-infall model including migration prescriptions has problems in reproducing the shape of the stellar distribution functions and in particular that of [Mg/Fe];

4. Despite the evidence found for stellar radial migration, it is difficult to give an estimation of the fraction of stars migrated to the solar vicinity from other part of the MW disc to explain the sample of Santos-Peral et al. (2020, 2021). Different prescriptions for radial migration have a small effect on the overall distribution functions, with different fractions of stars from inner and outer galactocentric rings giving similar overall results. Therefore, these are not good tools to impose constraints on migration. This leaves the door open for different conclusions about the contribution of migration on the MW disc (e.g., Vincenzo & Kobayashi 2020; Sharma et al. 2021). However, our results indicate that peculiar histories of star formation, such as that of the two-infall model are needed to explain the distribution of stars in the Galaxy, as also suggested by several works (e.g., Mackereth et al. 2018; Khoperskov et al. 2021, see also Vincenzo et al. 2021).

The above mentioned results highlight the importance of different ingredients in modelling the evolution of the solar vicinity. The choice of the stellar yields and the model star formation history, together with the implementation of secular evolution processes (i.e. stellar migration), have a central role in the reproduction of the available abundance and age constraints.

Acknowledgements. The authors thank the referee for the careful reading of the manuscript and the comments that significantly improve the quality of the manuscript. M.P. acknowledges the computing centre of CINECA and INAF under the coordination of the "accordo quadro MoU per lo svolgimento di attività congiunta di ricerca nuove frontiere in astrofsica: HPC e data exploration di nuova generazione" for the availability of computing resources. P.S.P. would like to thank the Centre National de Recherche Scientifique (CNRS) for the financial support, and partial support from the Université Côte d'Azur (UCA). P.S.P also acknowledges financial support by the Spanish Ministry of Science and Innovation through the research grant PID2019-107427GB-C31. This work has made use of data from the European Space Agency (ESA) mission *Gaia* (`https://www.cosmos.esa.int/gaia`), processed by the *Gaia* Data Processing and Analysis Consortium (DPAC, `https://www.cosmos.esa.int/web/gaia/dpac/consortium`). Funding for the DPAC has been provided by national institutions, in particular the institutions participating in the *Gaia* Multilateral Agreement.

References

Adibekyan, V. Z., Sousa, S. G., Santos, N. C., et al. 2012, A&A, 545, A32
Agertz, O., Renaud, F., Feltzing, S., et al. 2021, MNRAS, 503, 5826
Ahumada, R., Prieto, C. A., Almeida, A., et al. 2020, ApJS, 249, 3
Anders, F., Chiappini, C., Santiago, B. X., et al. 2014, A&A, 564, A115
Bailer-Jones, C. A. L., Rybizki, J., Fouesneau, M., Mantelet, G., & Andrae, R. 2018, AJ, 156, 58
Bressan, A., Marigo, P., Girardi, L., et al. 2012, MNRAS, 427, 127
Buck, T. 2020, MNRAS, 491, 5435
Buder, S., Lind, K., Ness, M. K., et al. 2019, A&A, 624, A19
Caffau, E., Bonifacio, P., Korotin, S. A., et al. 2021, A&A, 651, A20
Calura, F., & Menci, N. 2009, MNRAS, 400, 1347
Carrera, R., Bragaglia, A., Cantat-Gaudin, T., et al. 2019, A&A, 623, A80
Cescutti, G., Matteucci, F., François, P., & Chiappini, C. 2007, A&A, 462, 943
Chen, Y., Girardi, L., Bressan, A., et al. 2014, MNRAS, 444, 2525
Chen, Y., Bressan, A., Girardi, L., et al. 2015, MNRAS, 452, 1068
Chiappini, C., Matteucci, F., & Gratton, R. 1997, ApJ, 477, 765
Chiappini, C., Matteucci, F., & Romano, D. 2001, ApJ, 554, 1044
Chiappini, C., Anders, F., Rodrigues, T. S., et al. 2015, A&A, 576, L12
Clarke, A. J., Debattista, V. P., Nidever, D. L., et al. 2019, MNRAS, 484, 3476
de Laverny, P., Recio-Blanco, A., Worley, C. C., & Plez, B. 2012, A&A, 544, A126
de Laverny, P., Recio-Blanco, A., Worley, C. C., et al. 2013, The Messenger, 153, 18
De Pascale, M., Worley, C. C., de Laverny, P., et al. 2014, A&A, 570, A68
Di Matteo, P., Haywood, M., Combes, F., Semelin, B., & Snaith, O. N. 2013, A&A, 553, A102
Evans, D. W., Riello, M., De Angeli, F., et al. 2018, A&A, 616, A4
Feltzing, S., Bowers, J. B., & Agertz, O. 2020, MNRAS, 493, 1419
François, P., Matteucci, F., Cayrel, R., et al. 2004, A&A, 421, 613
Frankel, N., Rix, H.-W., Ting, Y.-S., Ness, M., & Hogg, D. W. 2018, ApJ, 865, 96
Freeman, K., & Bland-Hawthorn, J. 2002, ARA&A, 40, 487
Fuhrmann, K., Chini, R., Kaderhandt, L., & Chen, Z. 2017, MNRAS, 464, 2610
Gaia Collaboration (Brown, A. G. A., et al.) 2016, A&A, 595, A2
Gaia Collaboration (Brown, A. G. A., et al.) 2018, A&A, 616, A1
Gaia Collaboration (Brown, A. G. A., et al.) 2021, A&A, 649, A1
Grand, R. J. J., Bustamante, S., Gómez, F. A., et al. 2018, MNRAS, 474, 3629
Greggio, L. 2005, A&A, 441, 1055
Grisoni, V., Spitoni, E., Matteucci, F., et al. 2017, MNRAS, 472, 3637
Grisoni, V., Spitoni, E., & Matteucci, F. 2018, MNRAS, 481, 2570
Hayden, M. R., Bovy, J., Holtzman, J. A., et al. 2015, ApJ, 808, 132
Hayden, M. R., Recio-Blanco, A., de Laverny, P., Mikolaitis, S., & Worley, C. C. 2017, A&A, 608, L1
Haywood, M., Di Matteo, P., Lehnert, M. D., Katz, D., & Gómez, A. 2013, A&A, 560, A109
Haywood, M., Lehnert, M. D., Di Matteo, P., et al. 2016, A&A, 589, A66
Iwamoto, K., Brachwitz, F., Nomoto, K., et al. 1999, ApJS, 125, 439
Izzard, R. G., Preece, H., Jofre, P., et al. 2018, MNRAS, 473, 2984
Jofré, P., Heiter, U., Soubiran, C., et al. 2015, A&A, 582, A81
Jofré, P., Jorissen, A., Van Eck, S., et al. 2016, A&A, 595, A60
Johnson, J. W., Weinberg, D. H., Vincenzo, F., et al. 2021, MNRAS, 508, 4484
Kennicutt, R. C. Jr. 1998, ApJ, 498, 541
Khoperskov, S., Haywood, M., Snaith, O., et al. 2021, MNRAS, 501, 5176
Kobayashi, C., Umeda, H., Nomoto, K., Tominaga, N., & Ohkubo, T. 2006, ApJ, 653, 1145
Kobayashi, C., Karakas, A. I., & Umeda, H. 2011, MNRAS, 414, 3231
Kordopatis, G., Gilmore, G., Steinmetz, M., et al. 2013, AJ, 146, 134
Kordopatis, G., Binney, J., Gilmore, G., et al. 2015, MNRAS, 447, 3526
Kordopatis, G., Amorisco, N. C., Evans, N. W., Gilmore, G., & Koposov, S. E. 2016, MNRAS, 457, 1299
Kroupa, P., Tout, C. A., & Gilmore, G. 1993, MNRAS, 262, 545
Leung, S.-C., & Nomoto, K. 2020, ApJ, 888, 80
Limongi, M., & Chieffi, A. 2018, ApJS, 237, 13
Lindegren, L., Hernández, J., Bombrun, A., et al. 2018, A&A, 616, A2
Mackereth, J. T., Crain, R. A., Schiavon, R. P., et al. 2018, MNRAS, 477, 5072
Magrini, L., Randich, S., Kordopatis, G., et al. 2017, A&A, 603, A2
Maoz, D., & Graur, O. 2017, ApJ, 848, 25
Marigo, P., Girardi, L., Bressan, A., et al. 2017, ApJ, 835, 77
Martig, M., Rix, H.-W., Silva Aguirre, V., et al. 2015, MNRAS, 451, 2230
Matteucci, F. 2003, The Chemical Evolution of the Galaxy (Dordrecht: Kluwer Academic Publishers)
Matteucci, F. 2012, Chemical Evolution of Galaxies (Berlin Heidelberg: Springer-Verlag)
Matteucci, F., & Recchi, S. 2001, ApJ, 558, 351
Melioli, C., Brighenti, F., D'Ercole, A., & de Gouveia Dal Pino, E. M. 2009, MNRAS, 399, 1089
Miglio, A., Chiappini, C., Mackereth, J. T., et al. 2021, A&A, 645, A85
Mikolaitis, Š., Hill, V., Recio-Blanco, A., et al. 2014, A&A, 572, A33
Mikolaitis, Š., de Laverny, P., Recio-Blanco, A., et al. 2017, A&A, 600, A22
Minchev, I., Famaey, B., Combes, F., et al. 2011, A&A, 527, A147
Minchev, I., Chiappini, C., & Martig, M. 2013, A&A, 558, A9
Minchev, I., Anders, F., Recio-Blanco, A., et al. 2018, MNRAS, 481, 1645
Minchev, I., Matijevic, G., Hogg, D. W., et al. 2019, MNRAS, 487, 3946
Ness, M. K., Johnston, K. V., Blancato, K., et al. 2019, ApJ, 883, 177
Nidever, D. L., Bovy, J., Bird, J. C., et al. 2014, ApJ, 796, 38
Noguchi, M. 2018, Nature, 559, 585
Nomoto, K., Kobayashi, C., & Tominaga, N. 2013, ARA&A, 51, 457
Palla, M. 2021, MNRAS, 503, 3216
Palla, M., Matteucci, F., Spitoni, E., Vincenzo, F., & Grisoni, V. 2020a, MNRAS, 498, 1710
Palla, M., Matteucci, F., Calura, F., & Longo, F. 2020b, ApJ, 889, 4
Pastorelli, G., Marigo, P., Girardi, L., et al. 2019, MNRAS, 485, 5666

Pastorelli, G., Marigo, P., Girardi, L., et al. 2020, MNRAS, 498, 3283
Pinsonneault, M. H., Elsworth, Y., Epstein, C., et al. 2014, ApJS, 215, 19
Pinsonneault, M. H., Elsworth, Y. P., Tayar, J., et al. 2018, ApJS, 239, 32
Pouliasis, E., Di Matteo, P., & Haywood, M. 2017, A&A, 598, A66
Prantzos, N., Abia, C., Limongi, M., Chieffi, A., & Cristallo, S. 2018, MNRAS, 476, 3432
Queiroz, A. B. A., Anders, F., Chiappini, C., et al. 2020, A&A, 638, A76
Recio-Blanco, A., Bijaoui, A., & de Laverny, P. 2006, MNRAS, 370, 141
Recio-Blanco, A., de Laverny, P., Kordopatis, G., et al. 2014, A&A, 567, A5
Recio-Blanco, A., de Laverny, P., Allende Prieto, C., et al. 2016, A&A, 585, A93
Renaud, F., Agertz, O., Andersson, E. P., et al. 2021a, MNRAS, 503, 5868
Renaud, F., Agertz, O., Read, J. I., et al. 2021b, MNRAS, 503, 5846
Rojas-Arriagada, A., Recio-Blanco, A., de Laverny, P., et al. 2016, A&A, 586, A39
Romano, D., Chiappini, C., Matteucci, F., & Tosi, M. 2005, A&A, 430, 491
Romano, D., Karakas, A. I., Tosi, M., & Matteucci, F. 2010, A&A, 522, A32
Romano, D., Magrini, L., Randich, S., et al. 2021, A&A, 653, A72
Sanders, J. L., & Binney, J. 2015, MNRAS, 449, 3479
Santos-Peral, P., Recio-Blanco, A., de Laverny, P., Fernández-Alvar, E., & Ordenovic, C. 2020, A&A, 639, A140
Santos-Peral, P., Recio-Blanco, A., Kordopatis, G., Fernández-Alvar, E., & de Laverny, P. 2021, A&A, 653, A85
Schönrich, R., & Binney, J. 2009, MNRAS, 399, 1145
Seitenzahl, I. R., Ciaraldi-Schoolmann, F., Röpke, F. K., et al. 2013, MNRAS, 429, 1156
Sellwood, J. A., & Binney, J. J. 2002, MNRAS, 336, 785
Sharma, S., Hayden, M. R., & Bland-Hawthorn, J. 2021, MNRAS, 507, 5882
Sharma, S., Hayden, M. R., Bland-Hawthorn, J., et al. 2022, MNRAS, 510, 734
Silva Aguirre, V., Bojsen-Hansen, M., Slumstrup, D., et al. 2018, MNRAS, 475, 5487
Sousa, S. G., Santos, N. C., Mayor, M., et al. 2008, A&A, 487, 373
Sousa, S. G., Santos, N. C., Israelian, G., et al. 2011a, A&A, 526, A99
Sousa, S. G., Santos, N. C., Israelian, G., Mayor, M., & Udry, S. 2011b, A&A, 533, A141
Spitoni, E., & Matteucci, F. 2011, A&A, 531, A72
Spitoni, E., Matteucci, F., Recchi, S., Cescutti, G., & Pipino, A. 2009, A&A, 504, 87
Spitoni, E., Romano, D., Matteucci, F., & Ciotti, L. 2015, ApJ, 802, 129
Spitoni, E., Gioannini, L., & Matteucci, F. 2017, A&A, 605, A38
Spitoni, E., Silva Aguirre, V., Matteucci, F., Calura, F., & Grisoni, V. 2019, A&A, 623, A60
Spitoni, E., Verma, K., Silva Aguirre, V., & Calura, F. 2020, A&A, 635, A58
Spitoni, E., Verma, K., Silva Aguirre, V., et al. 2021, A&A, 647, A73
Sun, W. X., Huang, Y., Wang, H. F., et al. 2020, ApJ, 903, 12
Tang, J., Bressan, A., Rosenfield, P., et al. 2014, MNRAS, 445, 4287
Totani, T., Morokuma, T., Oda, T., Doi, M., & Yasuda, N. 2008, PASJ, 60, 1327
Vincenzo, F., & Kobayashi, C. 2020, MNRAS, 496, 80
Vincenzo, F., Weinberg, D. H., Miglio, A., Lane, R. R., & Roman-Lopes, A. 2021, MNRAS, 508, 5903
Woosley, S. E., & Weaver, T. A. 1995, ApJS, 101, 181
Yong, D., Casagrande, L., Venn, K. A., et al. 2016, MNRAS, 459, 487
Zhang, M., Xiang, M., Zhang, H.-W., et al. 2021, ApJ, 922, 145